Spin dynamics of 3*d* and 4*d* impurities embedded in prototypical topological insulators

Juba Bouaziz,* Manuel dos Santos Dias, Filipe Souza Mendes Guimarães, and Samir Lounis
Peter Grünberg Institut and Institute for Advanced Simulation, Forschungszentrum Jülich and JARA, 52425 Jülich, Germany

(Received 22 December 2018; revised manuscript received 20 March 2019; published 7 May 2019)

Topological insulators are insulating bulk materials hosting conducting surface states. Their magnetic doping breaks time-reversal symmetry and generates numerous interesting effects such as dissipationless transport. Nonetheless, their dynamical properties are still poorly understood. Here, we perform a systematic investigation of transverse spin excitations of 3*d* and 4*d* single impurities embedded in two prototypical topological insulators (Bi_2Te_3 and Bi_2Se_3). The impurity-induced states within the bulk gap of the topological insulators are found to have a drastic impact on the spin excitation spectra, resulting in very high lifetimes reaching up to microseconds. An intuitive picture of the spin dynamics is obtained by mapping onto a generalized Landau-Lifshitz-Gilbert phenomenological model. The first quantity extracted from this mapping procedure is the magnetic anisotropy energy, which is then compared to the one provided by the magnetic force theorem. This uncovers some difficulties encountered with the latter, which can provide erroneous results for impurities with a high density of states at the Fermi energy. Moreover, the Gilbert damping and nutation tensors are obtained. The nutation effects can lead to a non-negligible shift in the spin excitation resonance in the high-frequency regime. Finally, we study the impact of the surface state on the spin dynamics, which may be severely altered due to the repositioning of the impurity-induced state in comparison to the bulk case. Our systematic investigation of this series of magnetic impurities sheds light on their spin dynamics within topological insulators, with implications for available and future experimental studies.

DOI: 10.1103/PhysRevMaterials.3.054201

I. INTRODUCTION

The ever-increasing need for higher storage density oriented research towards the miniaturization of magnetic memories is constricted by the superparamagnetic limit [1]. The realization of smaller magnetic bits requires materials with a high magnetic anisotropy energy (MAE), originating from the relativistic spin-orbit interaction. The extreme limit for high-density magnetic storage consists of a single atomic bit [2], for which quantum effects can be predominant. Therefore, a deep fundamental understanding underlying the stability mechanisms is crucial for future technological applications. Moreover, the manipulation of these magnetic units relies on external time-dependent fields, with their dynamical properties being of prime relevance as well.

The standard tool for probing the dynamical magnetic properties (i.e., spin excitations) of single atoms is inelastic scanning tunneling spectroscopy (ISTS). It was employed to investigate magnetic adatoms on nonmagnetic surfaces [3–12]. The spin excitation signature in the differential conductance ($\frac{dI}{dV}$, with I being the tunneling current and V being the applied voltage) consists of steplike features at the excitation frequencies. They are determined by the applied external magnetic field and the MAE, which can also be accessed via other experimental methods such as x-ray magnetic circular dichroism [13,14]. The nature of both the substrate and the adsorbate plays a major role in the determination of the resonance frequency and lifetime of the excitation.

Several theoretical investigations of spin excitations of magnetic atoms deposited on nonmagnetic surfaces have been performed. In the limit of weak coupling (i.e., low hybridization) between the adsorbate and the substrate, the ISTS spectra can be interpreted employing a Heisenberg model with localized atomic moments possessing an integer (or half-integer) spin. Such a scenario occurs when the substrate is of insulating or semiconducting nature [6,15,16]. When the coupling to the substrate is strong, the hybridization effects must be taken into account and a more accurate description of the electronic structure is required. This was achieved using real-space first-principles calculations in the framework of the Korringa-Kohn-Rostoker Green's function (KKR-GF) method, which was extended to the dynamical regime [17–20] relying on time-dependent density functional theory (TD-DFT) in its linear response formulation [21].

Topological insulators are intermediate between metallic and insulating substrates, consisting of bulk insulators hosting conducting topologically protected surface states [22–24]. Magnetic impurities deposited on topological insulators were also investigated by means of scanning tunneling microscopy [13,25–28]. For instance, it was found in Ref. [27] that Fe impurities deposited on Bi_2Te_3 prefer to substitute a subsurface Bi atom after room-temperature annealing. It was also shown in Ref. [13] that, at low deposition temperature, Fe on Bi_2Te_3 may occupy hcp and fcc hollow sites while displaying an out-of-plane anisotropy. Nonetheless, an experimental analysis of their dynamical properties via ISTS, for example, is so far lacking. Furthermore, the magnetic doping of topological insulators breaks time-reversal symmetry and generates exotic phenomena such as the quantum anomalous

*j.bouaziz@fz-juelich.de

Hall effect [29,30]. In this case, one also expects a rather low but finite hybridization (with the surface state) in the region of the bulk gap, leading to unconventional dynamical behavior. For instance, the magnetization dynamics of a ferromagnet coupled to the surface state of a three-dimensional (3D) topological insulator has already been investigated, and an anomalous behavior in the ferromagnetic resonance was predicted [31]. Other studies with a similar focus were done in Refs. [32–35]. Furthermore, arrays of magnetic adatoms interacting with a topological surface state were considered in Ref. [36], with the surface magnons following a linear dispersion, very unusual for a ferromagnetic ground state. Moreover, the electron-spin resonance of single Gd ions embedded in Bi_2Se_3 was examined in Ref. [37]. The temperature dependence of the g factor was investigated and the coexistence of a metallic and an insulating phase (dual character) was reported.

In this paper, we systematically investigate the spin dynamics of $3d$ and $4d$ single impurities embedded in prototypical 3D topological insulators, namely, Bi_2Te_3 and Bi_2Se_3. Thin-film (with a topological surface state) and inversion symmetric bulk (insulating) geometries are considered. For an accurate description of the dynamical electronic properties of these impurities, we employ linear response TD-DFT as implemented in the KKR-GF method [17,18,20]. We compute the dynamical transverse magnetic susceptibility, which represents the magnetic response of the system to frequency-dependent transverse magnetic fields. It incorporates the density of spin excitations and can be connected to ISTS measurements [38]. The spin excitation spectra we obtain reveal astonishing results, with lifetimes spanning six orders of magnitude: from picoseconds to microseconds for Fe and Mn impurities embedded in Bi_2Se_3, respectively. These contrasting values of the lifetimes correlate with the presence (or absence) of in-gap states in the impurity local density of states (LDOS) near the Fermi energy [39]. Next we gain further insight on the magnetization dynamics by mapping the transverse dynamical magnetic susceptibility to the phenomenological Landau-Lifshitz-Gilbert (LLG) equation [40]. A generalized formulation of the LLG equation including tensorial Gilbert damping $\mathcal{G}$ and nutation $\mathcal{I}$ is employed [41]. The static limit of the response function via the LLG formulation was used to extract the MAE. The latter is then compared to the values obtained with conventional ground-state methods relying on the magnetic force theorem: band energy differences [42–44] and torque method [45]. A connection between the MAE obtained within the linear response theory and the torque method using small deviations is established. Moreover, for elements with high resonance frequencies, the signature of the nutation is observed as a resonance shift, proving that inertial effects are relevant at such high precession rates [41,46,47]. Finally, we compare the LLG parameters obtained when the $3d$ and $4d$ impurities are embedded in the bulk and at the surface of Bi_2Te_3. Our results show that the modification of the in-gap state due to the presence of the surface state may play a major role in the dynamics depending on the nature of the impurity.

This paper is structured as follows. Section II is dedicated to the description of the linear response TD-DFT approach employed to compute the spin excitation spectra. It also includes the mapping of the transverse dynamical magnetic susceptibility into the generalized phenomenological LLG model and the different methods used to compute the MAE. Section III is devoted to the analysis of the electronic structure and the ground-state properties of $3d$ and $4d$ transition-metal impurities embedded in Bi_2Te_3 and Bi_2Se_3. In Sec. IV, we present the MAE for the considered magnetic impurities and explain the discrepancies between the different methods. Section V contains a detailed discussion of the spin excitation spectra of $3d$ and $4d$ impurities embedded at the surface of both Bi_2Te_3 and Bi_2Se_3. The fitted LLG parameters are given as well, which are interpreted in terms of the impurity LDOS. Finally, in Sec. VI, the dynamical properties of the $3d$ impurities in the bulk and at the surface are compared. The contribution of the topological surface state for each impurity is then analyzed.

II. THEORETICAL DESCRIPTION

The description of the spin excitations of the investigated systems relies on linear response TD-DFT [17,20,21,48]. The central quantity in our approach is the dynamical magnetic susceptibility, which displays poles at the excitation energies of the system. The calculations are performed in two steps: First we determine the ground state of the system using conventional DFT calculations; then, we compute the dynamical response of the system to an external perturbing time-dependent magnetic field. To gain further physical insights into the results, we also describe how to map the results of TD-DFT calculations onto an extended phenomenological LLG model. Lastly, we compare the MAE obtained from the dynamical calculations with the ones computed from DFT calculations in different ways.

A. Density functional theory

The ground-state DFT simulations are done using the KKR-GF method [49,50] in the atomic sphere approximation including the full charge density, and the exchange-correlation potential is taken in the local spin-density approximation [51]. The spin-orbit interaction is included in a self-consistent fashion within the scalar relativistic approximation. Since we investigate impurities embedded in periodic crystals, we perform two types of calculations. The ground state of the clean host is determined first. Then, the impurities are self-consistently embedded in its crystalline structure. The host crystals investigated in this paper consist of Bi_2Te_3 and Bi_2Se_3. The bulk unit cell contains five atoms (one quintuple layer) in a rhombohedral structure (space group $R\bar{3}m$) [52]. The corresponding self-consistent calculations employ a $30 \times 30 \times 30$ k mesh. The surface is simulated using a slab containing six quintuple layers and 60×60 k points. For the impurity calculations, we consider a real-space cluster that contains 102 sites in total (24 Bi atoms, 31 Te (Se) atoms, and 47 vacuum sites). The magnetic impurities are substituting a Bi atom, which is located at the subsurface layer for the thin-film case [39]. Both experiment [27] and first-principles simulations [53] show that this position is thermodynamically stable for Fe in Bi_2Te_3. In addition to that, the nearest Te (Se) neighbors may relax their position getting closer to the

impurity [54]. These relaxations are not taken into account in the current paper.

B. Time-dependent density functional theory

The dynamical magnetic susceptibility encodes the spin excitation spectra. It describes the linear change in the spin magnetization density $\delta\vec{M}(\vec{r},\omega)$ upon the application of a frequency-dependent external magnetic field $\delta B(\vec{r},\omega)$ as

$$\delta M_\alpha(\vec{r},\omega) = \sum_\gamma \int d\vec{r}\,'\, \chi_{\alpha\gamma}(\vec{r},\vec{r}\,',\omega)\, \delta B_\gamma(\vec{r}\,',\omega), \quad (1)$$

where $\alpha,\gamma \in \{x,y,z\}$. For a specific direction of $\vec{M}(\vec{r})$, the susceptibility tensor can be divided into longitudinal and transversal blocks. In the presence of the spin-orbit interaction or magnetic noncollinearity, the two blocks are coupled. However, for the systems that we analyze in this paper, the coupling is negligible and we focus only on the transversal magnetic response of systems (the xy block when the magnetic moment is along the z direction). Within TD-DFT, the magnetic susceptibility $\chi_{\alpha\beta}(\vec{r},\vec{r}\,',\omega)$ is determined starting from the noninteracting magnetic susceptibility of the Kohn-Sham system, $\chi^{\mathrm{KS}}_{\alpha\beta}(\vec{r},\vec{r}\,',\omega)$, using a Dyson-like equation [17,20,21]:

$$\begin{aligned}\chi_{\alpha\beta}(\vec{r},\vec{r}\,',\omega) = \chi^{\mathrm{KS}}_{\alpha\beta}(\vec{r},\vec{r}\,',\omega) + \sum_{\gamma\mu=x,y}\int d\vec{r}_1\, d\vec{r}_2 \\ \times \chi^{\mathrm{KS}}_{\alpha\gamma}(\vec{r},\vec{r}_1,\omega)\, K^{\mathrm{xc}}_{\gamma\mu}(\vec{r}_1,\vec{r}_2,\omega) \\ \times \chi_{\mu\beta}(\vec{r}_2,\vec{r}\,',\omega), \end{aligned} \quad (2)$$

where $\alpha,\beta,\gamma,\mu \in \{x,y\}$ and $K^{\mathrm{xc}}_{\gamma\mu}(\vec{r},\vec{r}\,',\omega)$ is the transverse part of the exchange-correlation kernel, with $K^{\mathrm{xc}}_{\gamma\mu}(\vec{r},\vec{r}\,',\omega) = \delta_{\gamma\mu}K^{\mathrm{xc}}_{\perp}(\vec{r},\vec{r}\,',\omega)$. In the framework of the adiabatic local-density approximation (LDA) [21,55], $K^{\mathrm{xc}}_{\perp}(\vec{r},\vec{r}\,',\omega) = \delta(\vec{r}-\vec{r}\,')\,2B_{\mathrm{xc}}(\vec{r}\,)/M(\vec{r}\,)$ is frequency independent and local in space. The dynamical Kohn-Sham susceptibility is evaluated from the single-particle Green's function $\boldsymbol{G}(\vec{r},\vec{r}\,',\varepsilon)$ [defined in Eq. (B1)] as

$$\begin{aligned}\chi^{\mathrm{KS}}_{\alpha\beta}(\vec{r},\vec{r}\,',\omega) = -\frac{1}{\pi}\int_{-\infty}^{\varepsilon_{\mathrm{F}}} d\varepsilon\, \mathrm{Tr}\,\{\boldsymbol{\sigma}_\alpha\, \boldsymbol{G}(\vec{r},\vec{r}\,',\varepsilon+\omega+i0) \\ \times \boldsymbol{\sigma}_\beta\, \mathrm{Im}\,\boldsymbol{G}(\vec{r}\,',\vec{r},\varepsilon) + \boldsymbol{\sigma}_\alpha\, \mathrm{Im}\,\boldsymbol{G}(\vec{r},\vec{r}\,',\varepsilon) \\ \times \boldsymbol{\sigma}_\beta\, \boldsymbol{G}(\vec{r}\,',\vec{r},\varepsilon-\omega-i0)\}. \end{aligned} \quad (3)$$

Since the frequency range of interest is relatively low [20,48], the frequency dependence of the Kohn-Sham susceptibility is incorporated via a Taylor expansion as

$$\begin{aligned}\chi^{\mathrm{KS}}_{\alpha\beta}(\vec{r},\vec{r}\,',\omega) \approx \chi^{\mathrm{KS}}_{\alpha\beta}(\vec{r},\vec{r}\,',0) + \omega\,\frac{d\,\chi^{\mathrm{KS}}_{\alpha\beta}(\vec{r},\vec{r}\,',\omega)}{d\omega}\bigg|_{\omega=0} \\ + \frac{\omega^2}{2}\,\frac{d^2\chi^{\mathrm{KS}}_{\alpha\beta}(\vec{r},\vec{r}\,',\omega)}{d\omega^2}\bigg|_{\omega=0}, \end{aligned} \quad (4)$$

$\chi^{\mathrm{KS}}_{\alpha\beta}(\vec{r},\vec{r}\,',0)$ being the static Kohn-Sham susceptibility. Moreover, for a system with uniaxial symmetry, the transversal excitations can be summarized in the spin-flip magnetic susceptibility [20]:

$$\begin{aligned}\chi_{+-}(\vec{r},\vec{r}\,',\omega) = \tfrac{1}{4}[\chi_{xx}(\vec{r},\vec{r}\,',\omega) + i\chi_{xy}(\vec{r},\vec{r}\,',\omega) \\ - i\chi_{yx}(\vec{r},\vec{r}\,',\omega) + \chi_{yy}(\vec{r},\vec{r}\,',\omega)]. \end{aligned} \quad (5)$$

Further details on the computation of the Kohn-Sham susceptibility and exchange-correlation kernel can be found in Refs. [17,20,48]. Finally, we can obtain an intuitive picture of the spin excitations via the spatial average of $\chi_{+-}(\vec{r},\vec{r}\,',\omega)$ over a suitably defined volume enclosing the magnetic impurity:

$$\chi_{+-}(\omega) = \int_V d\vec{r} \int_V d\vec{r}\,'\, \chi_{+-}(\vec{r},\vec{r}\,',\omega), \quad (6)$$

which corresponds to its net response to a uniform external magnetic field [20].

C. Generalized Landau-Lifshitz-Gilbert equation

In order to develop a more intuitive picture of the magnetization dynamics, we make a connection with a phenomenological model for the magnetization dynamics. We consider a generalized formulation of the LLG equation [40] including a tensorial Gilbert damping $\underline{\mathcal{G}}$, as well as a nutation tensor $\underline{\mathcal{I}}$ accounting for inertial effects [41,56–58]. The latter can be important at relatively high frequencies [41,46,47]. The equation of motion of the magnetic moment $\vec{M}(t) = \int_V d\vec{r}\;\vec{M}(\vec{r},t)$ then reads

$$\frac{d\vec{M}}{dt} = -\gamma\,\vec{M}\times\left(\vec{B}^{\mathrm{eff}} + \underline{\mathcal{G}}\cdot\frac{d\vec{M}}{dt} + \underline{\mathcal{I}}\cdot\frac{d^2\vec{M}}{dt^2}\right). \quad (7)$$

Here γ is the gyromagnetic ratio ($\gamma = 2$ in atomic units) and $\vec{B}^{\mathrm{eff}}$ is the effective magnetic field acting on the magnetic moment. $\vec{B}^{\mathrm{eff}}$ can be split into two contributions: $\vec{B}^{\mathrm{eff}} = \vec{B}^{\mathrm{ext}} + \vec{B}^{\mathrm{a}}$, with $\vec{B}^{\mathrm{ext}}$ being the external magnetic field, and $\vec{B}^{\mathrm{a}}$ is an intrinsic anisotropy field which arises due to the spin-orbit interaction [20]. The relation between $\vec{B}^{\mathrm{a}}$ and the MAE $\mathcal{K}$ is detailed in Appendix A.

To establish a connection between the LLG equation and the transverse magnetic susceptibility computed using Eq. (2), we first consider that the local equilibrium direction is along the z axis and apply a small time-dependent transverse magnetic field:

$$\vec{B}^{\mathrm{ext}}(t) = \delta B_x(t)\,\vec{e}_x + \delta B_y(t)\,\vec{e}_y, \quad \text{with } \delta B_x(t),\, \delta B_y(t) \ll |\vec{B}^{\mathrm{a}}|. \quad (8)$$

Then, we linearize Eq. (7) with respect to transverse components of $\vec{B}^{\mathrm{ext}}(t)$ and $\vec{M}(t)$, which becomes, in the frequency domain,

$$\begin{aligned}\sum_{\beta=x,y}\left(\frac{B^{\mathrm{a}}_z}{M}\,\delta_{\alpha\beta} + \frac{i\omega}{\gamma M}\,\epsilon_{\alpha\beta} + i\omega\,\mathcal{G}_{\alpha\beta} + \omega^2\,\mathcal{I}_{\alpha\beta}\right)\delta M_\beta(\omega) \\ = \delta B_\alpha(\omega), \end{aligned} \quad (9)$$

with $\epsilon_{\alpha\beta}$ being the two-dimensional Levi-Civita symbol ($\epsilon_{xy} = +1$) and $\delta M_\beta(\omega)$ the β component of the frequency-dependent magnetization $\vec{M}(\omega)$. The preceding equation combined with Eq. (1) provides a direct connection between $\chi_{\alpha\beta}(\omega)$ obtained within TD-DFT and the phenomenological

LLG parameters:

$$[\chi_{xx}(\omega)]^{-1} = -\frac{2\mathcal{K}_{\text{Susc}}}{M^2} - \frac{i\omega}{\gamma M}\mathcal{G}^s_{\parallel} - \frac{\omega^2}{\gamma M}\mathcal{I}^s_{\parallel},$$
$$[\chi_{xy}(\omega)]^{-1} = \frac{i\omega}{\gamma M}(1+\mathcal{G}^a_{\parallel}) + \frac{\omega^2}{\gamma M}\mathcal{I}^a_{\parallel}, \tag{10}$$

where $\mathcal{K}_{\text{Susc}}$ is the MAE, and the subscript indicates that this quantity is extracted from the static magnetic susceptibility obtained from the TD-DFT calculations. $\mathcal{G}^s_{\parallel}$ ($\mathcal{I}^s_{\parallel}$) and $\mathcal{G}^a_{\parallel}$ ($\mathcal{I}^a_{\parallel}$) are the symmetric and antisymmetric components of the Gilbert damping (nutation) tensor, respectively. A more detailed description of the Gilbert damping and nutation tensors for the uniaxial symmetry that applies to the systems under consideration is provided in Appendix A. The previous equation shows in a clear fashion that the static limit of $\chi_{xx}(\omega)$ is inversely proportional to the anisotropy. In the limit of small nutation, the MAE is connected to the resonance frequency $\omega^{\text{LLG}}_{\text{res}}$ via (see Appendix A)

$$\omega^{\text{LLG}}_{\text{res}} = -\frac{\gamma}{\sqrt{1+(\mathcal{G}^s_{\parallel})^2+2\mathcal{G}^a_{\parallel}+(\mathcal{G}^a_{\parallel})^2}}\frac{2\mathcal{K}_{\text{Susc}}}{M_{\text{s}}}. \tag{11}$$

This is the resonance frequency for precessional motion about the z axis. Note that $\omega^{\text{LLG}}_{\text{res}}$ is renormalized by $\mathcal{G}^s_{\parallel}$ and $\mathcal{G}^a_{\parallel}$, accounting for the damping of the precession and the renormalization of γ, respectively [see Eq. (A7)].

D. Magnetocrystalline anisotropy

In the absence of external magnetic fields, the gap opening in the spin excitation spectrum is uniquely due to the MAE (i.e., anisotropy field) breaking the SU(2) rotational symmetry [20]. The expression of $\omega^{\text{LLG}}_{\text{res}}$ in the LLG model provided in Eq. (11) shows that the resonance frequency is proportional to $\mathcal{K}$, which can also be computed from ground-state DFT calculations. Here, we discuss two different ground-state methods to compute this quantity relying on the magnetic force theorem [42–44,59] and establish a connection with the MAE obtained using linear response theory, $\mathcal{K}_{\text{susc}}$.

For uniaxial systems, the energy depends on the direction of the magnetic moment in a simple way: $\mathcal{E}(\theta) \sim \mathcal{K}\cos^2\theta$, where θ is the angle that the magnetic moment makes with the z axis, i.e., $\vec{M}/|\vec{M}| = \hat{n}(\theta,\varphi) = (\cos\varphi\sin\theta, \sin\varphi\sin\theta, \cos\theta)$. To lowest order in the phenomenological expansion, the axial symmetry renders the energy independent of the azimuthal angle φ. It follows that the magnitude of the MAE, $\mathcal{K}$, can be obtained from total-energy differences for two different orientations of the magnetization (out of plane and in plane). However, as $\mathcal{K}$ is at most a few meV's, this approach requires very accurate total energies, which is computationally demanding.

Alternatively, one can use the magnetic force theorem, which states that, if the changes in the charge and magnetization densities accompanying the rotation of the spin moment are small, the total-energy difference can be replaced by the band energy difference [42–44]:

$$\mathcal{K}_{\text{Band}} = \mathcal{E}_{\text{Band}}(0^\circ) - \mathcal{E}_{\text{Band}}(90^\circ), \tag{12}$$

where $\mathcal{E}_{\text{Band}}(\theta)$ is the band energy (sum of Kohn-Sham energy eigenvalues) of the system when the spin moment makes an angle θ with the z axis:

$$\mathcal{E}_{\text{Band}}(\theta) = \int_{-\infty}^{\varepsilon_{\text{F}}} d\varepsilon\,(\varepsilon-\varepsilon_{\text{F}})\,\rho(\varepsilon;\theta). \tag{13}$$

It contains the effect of the orientation of the magnetic moment through the manner in which the density of states $\rho(\varepsilon;\theta)$ is modified upon its rotation. This quantity is evaluated with a single non-self-consistent calculation, by orienting the exchange-correlation magnetic field in the desired direction, $\vec{B}_{\text{xc}}(\vec{r}\,) = B_{\text{xc}}(\vec{r}\,)\,\hat{n}(\theta,\varphi)$ (rigid spin approximation [60]).

The MAE can also be evaluated from the magnetic torque, which corresponds to the first derivative of $\mathcal{E}_{\text{Band}}(\theta)$ with respect to the magnetic moment direction. Using the Hellman-Feynman theorem, the torque reads [45,61,62]

$$\mathcal{T}_\theta = \frac{\partial\mathcal{E}_{\text{Band}}}{\partial\theta} = \int d\vec{r}\; B_{\text{xc}}(\vec{r}\,)\,\frac{\partial\hat{n}(\theta,\varphi)}{\partial\theta}\cdot\vec{M}(\vec{r}\,;\theta). \tag{14}$$

As for the band energy calculations, the torque is also obtained from a single non-self-consistent calculation, under the same approximations. It is nonvanishing if the output spin magnetization density $\vec{M}(\vec{r}\,;\theta)$ is not collinear with the input magnetic moment direction. Considering the expected form of the MAE for uniaxial symmetry, we should find

$$\mathcal{T}_\theta = -\mathcal{K}_{\text{Torque}}\sin(2\theta). \tag{15}$$

In practice, the torque can be evaluated at different angles θ. In this paper, two deviation angles have been considered: a large deviation angle with $\theta = 45^\circ$, as done in Ref. [45], and a small one near self-consistency, $\theta = 5^\circ$. For such small deviations, one can connect $\mathcal{K}_{\text{Torque}}$ to the value of the MAE obtained from the magnetic susceptibility, $\mathcal{K}_{\text{Susc}}$. It is shown in Appendix B that, when considering a small rotation angle θ and a constant magnitude of the exchange-correlation spin splitting (frozen potential approximation),

$$\mathcal{K}_{\text{Susc}} = \frac{\mathcal{K}_{\text{Torque}}}{1-\frac{4\chi^{\text{KS}}_{+-}(0)\mathcal{K}_{\text{Susc}}}{M_z^2}} \sim \frac{\mathcal{K}_{\text{Torque}}}{1+\frac{B^{\text{a}}}{B_{\text{xc}}}}. \tag{16}$$

The previous expression shows that $\mathcal{K}_{\text{susc}}$ corresponds to the $\mathcal{K}_{\text{Torque}}$ (evaluated for a small deviation angle) renormalized by a prefactor $(1+\frac{B^{\text{a}}}{B_{\text{xc}}})^{-1}$. In fact, this result is similar to the renormalization observed for magnetic interactions computed from the magnetic susceptibility [63,64]. For the systems of interest ($3d$ and $4d$ transition-metal impurities), B^{a} is in the meV range while B_{xc} is in the order of eV. Therefore, one expects small corrections due to this renormalization, and the two quantities should be in good agreement.

III. ELECTRONIC STRUCTURE OF 3*d* AND 4*d* IMPURITIES IN Bi_2Te_3 AND Bi_2Se_3

In this section, we briefly recap the discussion of the electronic structure and ground-state properties of $3d$ impurities embedded in the Bi_2Te_3 (Bi_2Se_3) surface already addressed in Ref. [39]. Furthermore, we also consider $4d$ impurities which have a stronger hybridization with the host

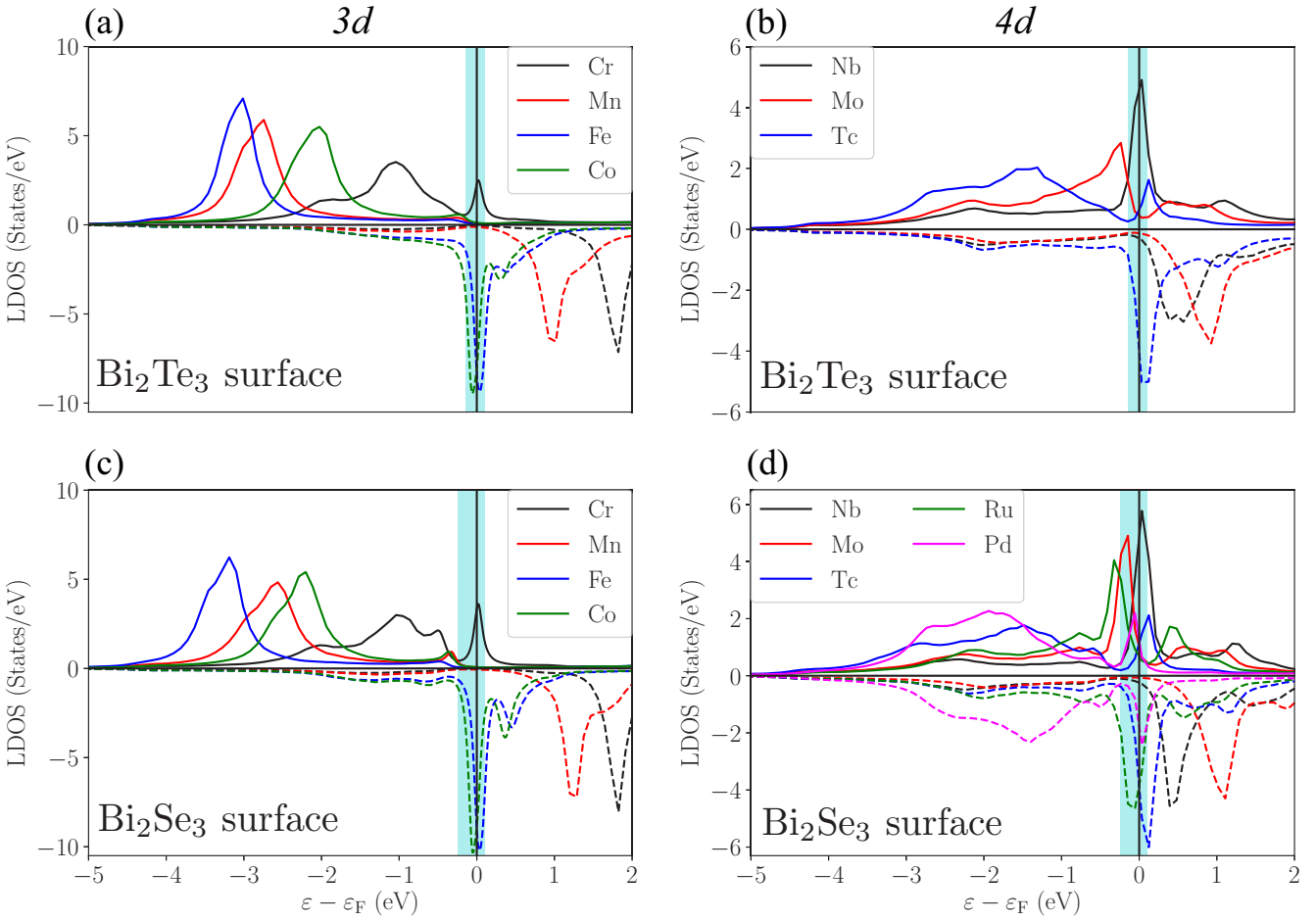

FIG. 1. Spin-resolved LDOS for 3*d* impurities (Cr, Mn, Fe, and Co) and 4*d* impurities (Nb, Mo, Tc, Ru, and Pd) embedded in a Bi_2Te_3 (Bi_2Se_3) surface. (a) 3*d* in Bi_2Te_3, (b) 4*d* in Bi_2Te_3, (c) 3*d* in Bi_2Se_3, and (d) 4*d* in Bi_2Se_3. The full lines represent the majority-spin states, with dashed lines for the minority-spin ones. The energies are given with respect to the Fermi energy ε_F and the energy window associated with the bulk band gap is highlighted with light blue color.

electrons compared to the 3*d* ones. This information will be employed for the analysis of their dynamical properties, such as the Gilbert damping. The LDOS of 3*d* and 4*d* magnetic impurities embedded into Bi_2Te_3 and Bi_2Se_3(111) surfaces are shown in Fig. 1. The bulk band gap (Δ_{gap}) is depicted in light blue, with $\Delta_{gap} \approx 0.25$ eV for Bi_2Te_3 and $\Delta_{gap} \approx 0.35$ eV for Bi_2Se_3. These values are in line with the results obtained using LDA+GW [65] and with the experimental data [66,67]. We consider that the impurity spin moment is oriented perpendicularly to the surface (i.e., along the [111] direction). The full lines represent the majority-spin channel (↑), while the dashed lines account for the minority-spin channel (↓). All the 3*d* and 4*d* impurities donate electrons to the host atoms (see Table I). It can also be seen in Fig. 1 that the spin splitting of the 4*d* impurities is weaker compared to the 3*d* ones, resulting in smaller spin moments, as listed in Table I. This is attributed to the Stoner parameter being larger for 3*d* than for 4*d* elements [68].

All 3*d* elements except Cr display a completely filled majority-spin *d* resonance. Mn and Cr have a nearly empty

TABLE I. Ground-state properties of 3*d* and 4*d* impurities embedded in the Bi_2Te_3 and Bi_2Se_3 surfaces including the valence charge on the impurity $\mathcal{Q}$, spin moment M_s, and orbital moment M_l. The spin and orbital moments are given in units of μ_B.

		Cr	Mn	Fe	Co	Nb	Mo	Tc	Ru	Pd
$\mathcal{Q}$	Bi_2Te_3	5.154	6.160	7.282	8.448	3.488	4.717	5.892	7.147	9.421
	Bi_2Se_3	4.841	5.863	6.963	8.136	3.077	4.316	5.474	6.734	9.041
M_s	Bi_2Te_3	3.843	4.412	3.395	2.108	1.097	2.678	2.493	0.000	0.000
	Bi_2Se_3	3.671	4.421	3.482	2.231	0.906	2.574	2.534	0.564	0.578
M_l	Bi_2Te_3	0.065	0.050	0.260	0.883	–0.143	–0.004	0.202	0.000	0.000
	Bi_2Se_3	0.008	0.024	0.144	0.942	–0.048	–0.093	0.079	0.378	0.135

minority-spin d resonance, resulting in a large spin moment and a small orbital moment (M_l). Fe and Co have a partially filled minority-spin d resonance, leading to higher values for M_l, as shown in Table I. The LDOS also reveals impurity-induced in-gap states near the Fermi energy, which arise from the hybridization with the bulk sp states of Bi_2Te_3 (Bi_2Se_3) [39]. When replacing the Bi_2Te_3 host by Bi_2Se_3, the valence charge and the spin moment are mildly affected, in contrast to the orbital moments which are considerably altered [39].

For 4d impurities, both minority- and majority-spin d resonances are partially occupied due to a weak spin splitting. The LDOS is broader and flatter in comparison with the 3d ones, indicating a stronger hybridization with the host material, as the 4d orbitals are spatially more extended than the 3d ones, and so overlap more with the orbitals of the host. In the Bi_2Te_3 host, Nb, Mo, and Tc are found to be magnetic, while Ru, Rh, and Pd impurities were found to be nonmagnetic. The analysis of the paramagnetic LDOS (not shown here) reveals that, when moving in the periodic table from Tc towards Pd (i.e., adding electrons), the 4d peak is shifted to lower energies. This leads to a drastic decrease of the LDOS at ε_F and makes the Stoner criterion unfulfilled. Nb has a less than half-filled d shell, inducing an orbital moment antiparallel to its spin moment, as shown in Table I. For Mo and Tc, a half-filled d shell results in the highest values for M_s between the 4d elements. These observations are in qualitative agreement with Hund's rules [69]. In-gap states are also observed near ε_F, as for the 3d impurities. Interestingly, in the Bi_2Se_3 host, Ru and Pd acquire a magnetic moment, while Rh remains nonmagnetic. Higher values of the LDOS at ε_F compared to the Bi_2Te_3 host now satisfy the Stoner criterion for these elements. Pd is a rather peculiar case, since the increase of the LDOS at ε_F is related to the presence of an in-gap state in the minority-spin LDOS, as shown in Fig. 1(d).

The electronic structure, especially in the vicinity of the Fermi energy, governs the behavior of the MAE and spin excitations of the system. In particular, the presence of d resonances near ε_F may result in inaccuracies in the computation of the MAE. Together with in-gap states, it can also induce high values of the Gilbert damping, as discussed in the next sections.

IV. MAGNETOCRYSTALLINE ANISOTROPY OF 3d AND 4d IMPURITIES IN Bi_2Te_3 AND Bi_2Se_3

We now investigate the MAE employing the different methods discussed in Sec. II D. In our convention, a positive (negative) MAE stands for an in-plane (out-of-plane) easy axis. In Fig. 2(a), we show the evolution of the MAE for 3d impurities embedded in Bi_2Te_3 and Bi_2Se_3, respectively. For every impurity, all the methods predict the same easy axis. In the Bi_2Te_3 host, Cr and Fe present an in-plane magnetic anisotropy, while Mn and Co favor an out-of-plane orientation. The trend is mostly accounted for by Bruno's formula [70], where the MAE is given by the anisotropy of the orbital moment (M_l): $\mathcal{K} \propto \zeta^2 (M_l^x - M_l^z)$, with ζ being the spin-orbit interaction strength. Mn displays a small MAE, as it has a small orbital moment, while the large anisotropy energies obtained for Fe and Co stem both from their large orbital moments and their substantial dependence on the spin orientation. However, the results obtained for the MAE of Cr do not agree with the predictions of Bruno's formula, since the MAE reaches ∼1 meV, despite a rather small anisotropy in the orbital moment of the adatom (see Table II). For the Bi_2Se_3 host, the anisotropy follows very similar trends in comparison with the Bi_2Te_3 case. Nonetheless, the easy axis of Cr switches from in plane to out of plane, while the MAE of Fe and Co present a noticeable increase, as shown in Fig. 2(a). These changes in the MAE are attributed to the modification of the ground-state properties, particularly the orbital moments (as listed in Table II), according to Bruno's formula.

In Fig. 2(b), we show the MAE of 4d impurities embedded in Bi_2Te_3 and Bi_2Se_3 computed with the different approaches outlined in Sec. II D. For the Bi_2Te_3 case, all the impurities

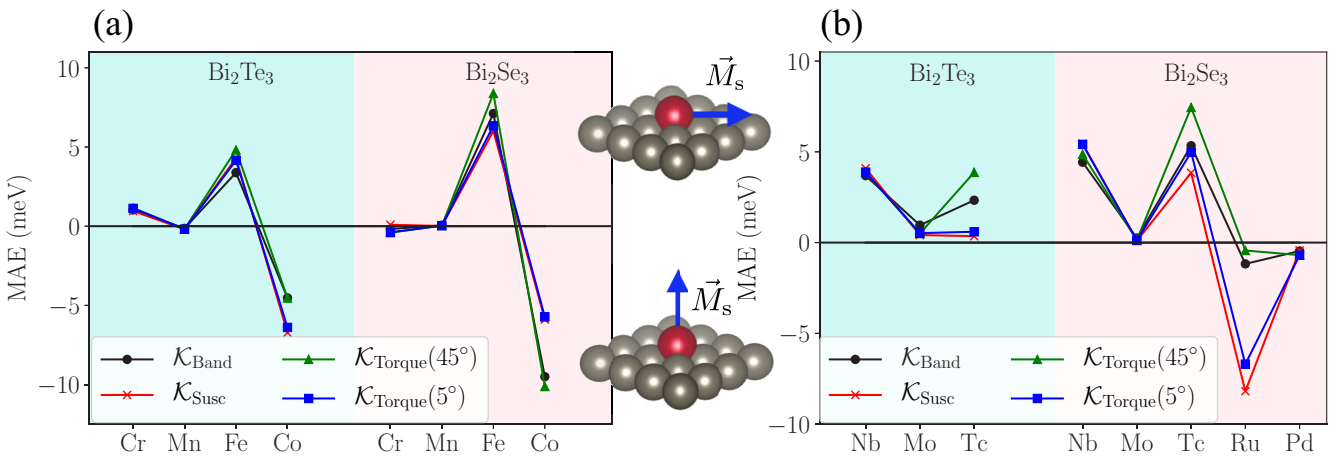

FIG. 2. Comparison of the MAE for (a) 3d impurities and (b) 4d impurities, embedded in a Bi_2Te_3 and a Bi_2Se_3 surface. The black curve is obtained using the band energy differences [$\mathcal{K}_{Band}$, Eq. (12)] (with a 90° rotation of the spin moment). The red curve shows the MAE computed from the static part of the magnetic susceptibility [$\mathcal{K}_{Susc}$, Eq. (10)]. The green and blue curves are obtained using the torque method at 45° and 5° [$\mathcal{K}_{Torque}(\theta)$, Eq. (14)], respectively. Most of the impurities display an in-plane magnetic anisotropy ($\mathcal{K} > 0$).

TABLE II. Change in the valence charge of the impurity $\Delta\mathcal{Q}^{zx}$, spin moment $\Delta M_{\rm s}^{zx}$, and orbital moment $\Delta M_{\rm l}^{zx}$ for 3*d* and 4*d* impurities embedded in a Bi_2Te_3 and a Bi_2Se_3 surface, using the frozen potential approximation. For Fe and Co, $\Delta\mathcal{Q}^{zx}$ and $\Delta M_{\rm s}^{zx}$ are relatively large, invalidating the use of the magnetic force theorem to compute the MAE.

		Cr	Mn	Fe	Co	Nb	Mo	Tc	Ru	Pd
$\Delta\mathcal{Q}^{zx}$	Bi_2Te_3	–0.016	0.001	–0.224	–0.484	0.018	0.002	–0.287	0.000	0.000
	Bi_2Se_3	–0.001	0.000	–0.320	–0.583	–0.004	0.001	–0.319	–0.347	0.000
$\Delta M_{\rm s}^{zx}$	Bi_2Te_3	–0.016	–0.001	0.224	0.483	0.015	–0.000	0.288	0.000	0.000
	Bi_2Se_3	–0.001	–0.000	0.320	0.582	–0.009	0.001	0.286	0.320	–0.003
$\Delta M_{\rm l}^{zx}$	Bi_2Te_3	0.019	0.003	–0.323	0.484	–0.081	–0.002	–0.188	0.000	0.000
	Bi_2Se_3	0.003	0.002	–0.493	0.487	–0.261	0.003	–0.284	0.285	0.008

(Nb, Mo, and Tc) display an in-plane easy axis. Nb displays a large MAE, while Mo and Tc have a rather small one [with the exception of $\mathcal{K}_{\rm Torque}(45^\circ)$ and $\mathcal{K}_{\rm Band}$]. For Mo, the small MAE correlates with its small orbital moment. In the Bi_2Se_3 host, Nb, Mo, and Tc are characterized by an in-plane easy axis as well. Note that, due to a strong hybridization with the host [broad LDOS in Figs. 1(b) and 1(d)], the MAE of Tc is drastically affected by the surrounding environment. Ru and Pd acquire a magnetic moment in Bi_2Se_3 displaying an out-of-plane easy axis. Particularly, Ru displays a very large MAE in comparison with the rest of the 4*d* elements.

We now focus on the reasons why different methods may provide contrasting values for the MAE (see Fig. 2). The origin of these divergences can be traced back to the features of the electronic structure at the impurity site. Figure 2(a) shows that the obtained MAEs of Fe and Co can be separated in two groups, according to the method used to compute them: one for large angle methods, including the band energy differences [$\mathcal{K}_{\rm Band}$, Eq. (12)] and the torque method at 45° [$\mathcal{K}_{\rm Torque}(45^\circ)$, Eq. (14)], and the other for small perturbations, encompassing the torque method at 5° [$\mathcal{K}_{\rm Torque}(5^\circ)$, Eq. (14)] and linear response theory [$\mathcal{K}_{\rm Susc}$, Eq. (10)]. The results from the two methods in each group are in good agreement with each other, but the results from one group do not agree with those from the other. This can be understood via Table II, which lists the change in the ground-state properties of the impurity upon 90° rotation of the spin moment ($z \to x$ axis), in a frozen potential calculation. There is a large variation in the valence charge and in the spin moment of Fe and Co in comparison to Cr and Mn, owing to the change in the position of the 3*d* peak in the minority-spin channel in the vicinity of $\varepsilon_{\rm F}$ [see Figs. 1(a) and 1(c)]. This violates the assumptions justifying the magnetic force theorem (in the frozen potential approximation), as previously observed in Ref. [71] for Co adatoms deposited on a Cu(111) surface. The disagreement between the different methods for Tc and Ru observed in Fig. 2(b) is attributed to a high occupation at $\varepsilon_{\rm F}$ as well [see Figs. 1(b) and 1(d)]. An exception occurs for Nb, where good agreement between the different methods is observed. In this case, the high LDOS at $\varepsilon_{\rm F}$ is due to the majority-spin states, which are weakly affected by the spin rotation.

The previous analysis indicates that, if a high density of electronic states is present at $\varepsilon_{\rm F}$ (Fe, Co, Tc, and Ru), a large rotation angle may lead to large changes in the charge density and invalidate the use of the magnetic force theorem in combination with the frozen potential approximation. As discussed in Sec. II D and in Appendix B, the gap in the spin excitation spectra as measured with ISTS defined by $\mathcal{K}_{\rm Susc}$ is very well described by $\mathcal{K}_{\rm Torque}(\theta)$ obtained with small rotation angles (in our case, $\theta = 5^\circ$).

V. SPIN EXCITATIONS OF 3*d* AND 4*d* IMPURITIES IN Bi_2Te_3 AND Bi_2Se_3

In Sec. III, we addressed the ground-state properties of 3*d* and 4*d* impurities embedded in Bi_2Te_3 and Bi_2Se_3. Here, we investigate their spin dynamics, relate it to the MAE obtained in Sec. IV, and study the possibility of exciting and manipulating these impurities with time-dependent external magnetic fields. We focus on the transverse spin excitations encoded in the dynamical magnetic susceptibility, which have been observed experimentally for magnetic impurities on nonmagnetic surfaces by means of ISTS measurements [3,8,9,11,72,73]. In these experiments, the spin excitations yield a step in the differential tunneling conductance at well-defined energies.

We show in Fig. 3 the imaginary part of $\chi_{+-}(\omega)$ (i.e., the density of states of the magnetic excitations) as a function of the frequency of the external field for both 3*d* and 4*d* impurities embedded in Bi_2Te_3 and Bi_2Se_3. Only the response of the magnetic impurities is considered, since the induced moments in the surrounding (host) atoms are rather small. Nonetheless, their contribution is accounted for when computing the transverse exchange-correlation kernel $K_\perp^{\rm xc}$ at the impurity site via the spin-splitting sum rule [17,20]. The LLG parameters obtained by fitting the data to Eq. (10) are given in Table III. As depicted in Fig. 3, Im $\chi_{+-}(\omega)$ has a Lorentzian-like shape, and the resonance frequency ($\omega_{\rm res}$) is finite even in the absence of an external magnetic field. This resonance arises from the MAE, which breaks the SU(2) rotational symmetry (i.e., no Goldstone mode), as explained previously in Sec. II D. The highest resonance frequencies are obtained for Nb and Ru due to their strong anisotropy combined with a small magnetic moment complying with Eq. (11), while the smallest value of $\omega_{\rm res}$ is obtained for Mn impurities in Bi_2Se_3. The dashed lines in Fig. 3 represent the resonance position obtained neglecting dynamical corrections in Eq. (11), leading to the estimate $\omega_{\rm res}^0 = -\frac{2\gamma\mathcal{K}_{\rm Susc}}{M_{\rm s}}$ (with $\gamma = 2$ and $\underline{\mathcal{G}} = 0$) [20]. There is a qualitative agreement between $\omega_{\rm res}^0$ and the resonance position extracted from the spin excitation spectra, $\omega_{\rm res}$, including damping and nutation. Nonetheless, their values are

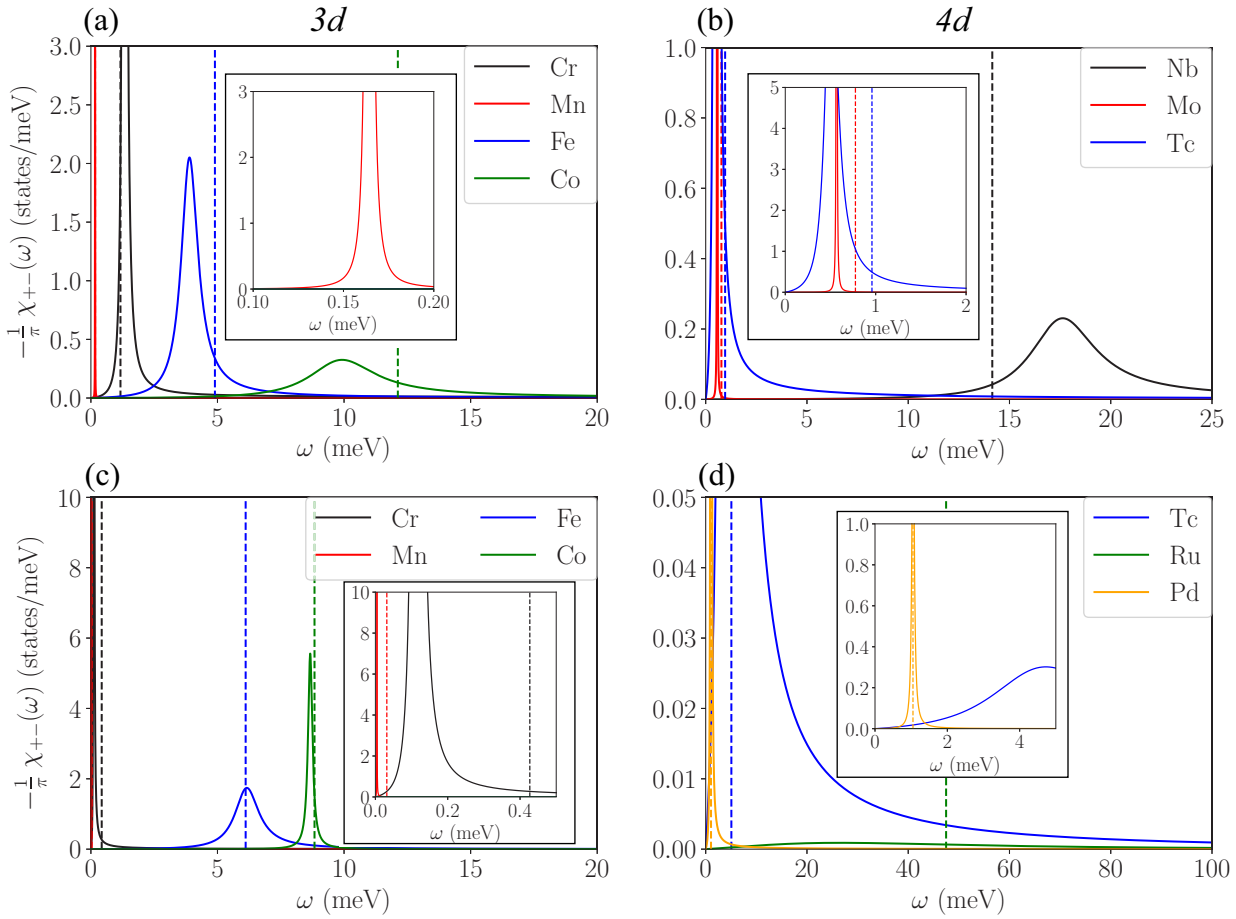

FIG. 3. Density of states of transverse spin excitations for magnetic impurities. The panels show the results for (a) 3*d* and (b) 4*d* impurities embedded in Bi_2Te_3 and for (c) 3*d* and (d) 4*d* impurities embedded in Bi_2Se_3. They present an almost Lorentzian shape, with resonances located at the excitation energies of the system. The dashed lines mark the resonance frequency without dynamical corrections, $\omega^0_{\rm res} = -\frac{2\gamma K_{\rm Susc}}{M_s}$. For Mn, Co, Ru, and Pd, $\chi_{-+}(\omega)$ is plotted instead, to account for their easy-plane MAE.

quantitatively different, illustrating that dynamical corrections can be of crucial importance for an accurate determination of the resonance frequency.

Another quantity which is strongly dependent on the nature of the impurity and the host is the full width at half maximum Γ. This quantity is proportional to the symmetric part of the Gilbert damping tensor ($\mathcal{G}^s_\parallel$) and provides information about the lifetime of the excitations [74] as $\tau = \frac{2}{\Gamma}$. This lifetime ranges from picoseconds (comparable to lifetimes obtained at metallic surfaces [20,74]) to very high values reaching microseconds for Mn in Bi_2Se_3 as shown in Fig. 4. Furthermore, the values of $\mathcal{G}^s_\parallel$, shown in Table III, can be interpreted in terms of the LDOS at ε_F, since $\mathcal{G}^s_\parallel \propto n^\downarrow(\varepsilon_F)\, n^\uparrow(\varepsilon_F)$ [where $n^\downarrow(\varepsilon)$ and $n^\uparrow(\varepsilon)$ represent the LDOS of the minority- and majority-spin channels, respectively] [48]. The highest values of $\mathcal{G}^s_\parallel$ are obtained for Ru, which coincide with the lowest excitation lifetime as displayed in Fig. 4. The antisymmetric part of the Gilbert damping tensor $\mathcal{G}^a_\parallel$ is also displayed in Table III. It accounts for the renormalization of the gyromagnetic ratio, $\gamma_{\rm eff} = \frac{\gamma}{1+\mathcal{G}^a_\parallel}$ (see Appendix A). This renormalization is attributed to the presence of a finite LDOS at ε_F as well [48]. $\mathcal{G}^a_\parallel$ is negative for Cr, Nb, and Ru, indicating an enhancement of the gyromagnetic ratio (i.e., $\gamma_{\rm eff} > 2$), while $\gamma_{\rm eff} < 2$ for the remaining impurities. Note that the spin excitation spectra of Nb and Mo impurities in Bi_2Se_3 are not shown in Fig. 3, since for these elements the Taylor expansion shown in Eq. (4) fails due to contributions from higher-order terms in frequency becoming too large.

The importance of the nutation can be estimated from the real part of the denominator of Eq. (A5). Both damping and nutation terms, $\mathcal{G}^a_\parallel\omega$ and $\mathcal{I}^s_\parallel\omega^2$, contribute to the resonance. When it occurs at frequencies higher than $\omega_c = \frac{\mathcal{G}^a_\parallel}{\mathcal{I}^s_\parallel}$, $\omega_{\rm res}$ can be substantially affected by the nutation. The ratio between $\omega^{\rm LLG}_{\rm res}$ obtained using Eq. (11) (without including nutation) and ω_c (shown in Table III) is employed to evaluate the importance of this contribution. The symmetric parts of the Gilbert damping and nutation tensors can be also related via $\mathcal{I}^s_\parallel \propto \mathcal{G}^s_\parallel$ [47,56], i.e., the damping and nutation coefficients are proportional. The ratio ω_c is fairly small for the majority of the elements, indicating that nutation has no significant impact on the resonant spin precession. However, for some elements such as Nb and Tc (in Bi_2Se_3) the nutation leads to a shift of $\sim$1.3 and 0.4 meV in the resonance frequency, respectively. Finally, the most striking element is once again Ru, with a shift of the resonance frequency from $\omega^{\rm LLG}_{\rm res} = 55.49$ to $\omega_{\rm res} = 25.52$ due to the nutation.

TABLE III. LLG parameters for 3*d* and 4*d* impurities embedded in the surface of Bi_2Te_3 (Bi_2Se_3), obtained by fitting the TDDFT dynamical susceptibility data to Eq. (10). M_s is the spin moment of the impurity. $\mathcal{G}_\parallel^s$ is the symmetric part and $\mathcal{G}_\parallel^a$ is the antisymmetric part of the damping tensor, both unitless. $\mathcal{K}_{\text{Susc}}$ is the MAE obtained from the magnetic susceptibility, in meV. $\omega_{\text{res}}^{\text{LLG}}$ is the resonance frequency without including nutation, in meV, as defined in Eq. (11). A large ratio between $\omega_{\text{res}}^{\text{LLG}}$ and $\omega_c = \frac{\mathcal{G}_\parallel^a}{\mathcal{I}_\parallel^s}$ indicates that the nutation makes a substantial contribution to ω_{res}, while $\eta_c = \frac{\mathcal{G}_\parallel^s}{\mathcal{I}_\parallel^a}$ provides information on the contribution of the nutation to the damping of the spin excitation. Ru and Pd in Bi_2Te_3 were found to be nonmagnetic, so the corresponding entries are marked with a dash.

		Cr	Mn	Fe	Co	Nb	Mo	Tc	Ru	Pd
M_s	Bi_2Te_3	3.844	4.412	3.395	2.109	1.097	2.678	2.493	–	–
	Bi_2Se_3	3.671	4.421	3.482	2.231	0.906	2.574	2.534	0.564	0.578
$\mathcal{G}_\parallel^s$	Bi_2Te_3	0.019	0.000	0.143	0.164	0.053	0.000	0.172	–	–
	Bi_2Se_3	0.037	0.000	0.112	0.012	0.003	0.000	0.512	0.852	0.094
$\mathcal{G}_\parallel^a$	Bi_2Te_3	–0.245	0.109	0.286	0.274	–0.087	0.096	0.099	–	–
	Bi_2Se_3	–0.153	0.101	0.125	0.196	–0.021	0.134	0.081	–0.396	1.824
ω_c	Bi_2Te_3	77.68	3439	135.7	277.4	21.91	224.5	31.64	–	–
	Bi_2Se_3	283.2	1340	100.4	73.37	2.784	403.5	4.481	10.11	437.0
η_c	Bi_2Te_3	7.154	298.3	65.66	38.39	30.36	752.2	234.4	–	–
	Bi_2Se_3	30.97	17820	76.31	40.19	8.703	171.5	84.93	341.8	502.5
$\mathcal{K}_{\text{Susc}}$	Bi_2Te_3	0.959	–0.201	4.302	–6.725	4.091	0.417	0.353	–	–
	Bi_2Se_3	0.090	0.005	6.019	–5.894	5.453	0.102	3.845	–8.178	–0.431
$\omega_{\text{res}}^{\text{LLG}}$	Bi_2Te_3	1.322	0.164	3.917	9.926	16.31	0.568	0.509	–	–
	Bi_2Se_3	0.115	0.004	6.113	8.833	24.08	0.158	5.073	55.49	1.055
$\frac{\omega_{\text{res}}^{\text{LLG}}}{\omega_c}$	Bi_2Te_3	0.017	0.000	0.029	0.036	0.744	0.003	0.016	–	–
	Bi_2Se_3	0.000	0.000	0.063	0.125	8.836	0.000	1.132	5.487	0.002

VI. SURFACE AND BULK SPIN DYNAMICS

We now compare different cases of 3*d* and 4*d* magnetic impurities embedded in a surface and in a bulk inversion symmetric Bi_2Te_3 (i.e., insulating phase with no topological surface state). This enables us to disentangle the surface and bulk contributions to the spin dynamics. The analysis of the ground-state properties of the 3*d* impurities embedded in bulk Bi_2Te_3 is given in Ref. [39]. The impurity-induced electronic in-gap states are also present in 4*d* impurities embedded in bulk Bi_2Te_3. The LLG parameters obtained in the bulk (denoted with a subscript "b") and at the surface (denoted with a subscript "s") are displayed in Table IV. With the exception of Mn, the MAE obtained from the susceptibility differs considerably between the bulk and surface cases—Cr even has its easy axis switched. The overall change in the MAE is a decrease from the surface to the bulk cases. Since the magnetic atoms are substituting a Bi atom (which is located in the subsurface layer for the thin-film setup), the immediate environment of the embedded impurities is the same in bulk and at the surface. However, for the bulk case, the missing contribution of the surface state leads to modifications in the electronic structure, altering the virtual bound and the in-gap states [39]. This results in a reduction of the MAE. The spectral weight at the Fermi level is also affected, leading to a modification of the damping parameter [48]. For Cr, Fe, and Tc, $\mathcal{G}_\parallel^s$ decreases, while for Co, Nb, and Mo it increases. $\mathcal{G}_\parallel^a$ follows similar trends as in the surface case. Co and Nb are the exception since $\mathcal{G}_\parallel^a$ switches sign, resulting in a change of γ_{eff}. The nutation is negligible for most of elements, except for Nb and Co—for the latter, it leads to a noticeable shift of the resonance frequency from $\omega_{\text{res}}^{\text{LLG}} = 4.24$ meV to $\omega_{\text{res}} = 4.68$ meV. In summary, Co and Nb impurities are very sensitive to the the presence of the surface state, where the impurity states display rather different behaviors in the bulk and at the surface leading to a different spin excitational nature. In contrast, Mn impurities have a similar behavior in the bulk and at the surface, showing that the topological surface state plays a negligible role for their spin dynamics.

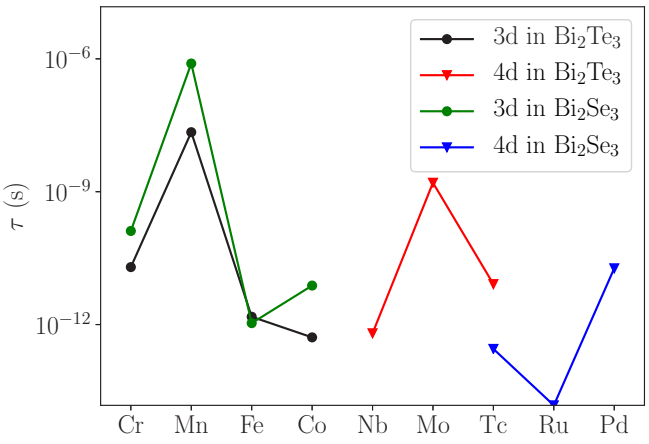

FIG. 4. Excitation lifetime of 3*d* and 4*d* magnetic impurities embedded in Bi_2Te_3 and Bi_2Se_3. Note that the lifetime axis is on a logarithmic scale. The highest excitation lifetime is obtained for Mn in Bi_2Se_3 and reaches microseconds, while the lowest one is obtained for Ru. Elements without data were found to be nonmagnetic in the respective hosts.

VII. CONCLUSIONS

In this paper, we employed a first-principles approach for the investigation of the spin excitation spectra of 3*d* and 4*d*

TABLE IV. LLG parameters for 3*d* and 4*d* impurities embedded in the surface (subscript s) and in the bulk (subscript b) of Bi_2Te_3, obtained by fitting the TDDFT dynamical susceptibility data to Eq. (10). M_s is the spin moment of the impurity. $\mathcal{G}^s_\parallel$ is the symmetric part and $\mathcal{G}^a_\parallel$ is the antisymmetric part of the damping tensor, both unitless. $\mathcal{K}_{\rm Susc}$ is the MAE obtained from the magnetic susceptibility, in meV. $\omega^{\rm LLG}_{\rm res}$ is the resonance frequency without including nutation, in meV, as defined in Eq. (11). A large ratio between $\omega^{\rm LLG}_{\rm res}$ and $\omega_c = \frac{\mathcal{G}^a_\parallel}{\mathcal{I}^s_\parallel}$ indicates that the nutation makes a substantial contribution to $\omega_{\rm res}$, while $\eta_c = \frac{\mathcal{G}^s_\parallel}{\mathcal{I}^a_\parallel}$ provides information on the contribution of the nutation to the damping of the spin excitation. The MAE and the Gilbert damping are considerably affected when going from surface to bulk. The largest changes occur in the case of the Co impurity.

	M_s	$\mathcal{G}^s_\parallel$	$\mathcal{G}^a_\parallel$	ω_c	η_c	$\mathcal{K}_{\rm Susc}$	$\omega^{\rm LLG}_{\rm res}$	$\frac{\omega^{\rm LLG}_{\rm res}}{\omega_c}$
Cr_s	3.844	0.018	–0.245	77.68	7.154	0.959	1.322	0.017
Cr_b	3.823	0.004	–0.215	332.6	47.48	–0.824	1.090	0.003
Mn_s	4.412	0.000	0.109	3439	298.4	–0.201	0.164	0.000
Mn_b	4.335	0.000	0.118	860.7	590.4	–0.216	0.178	0.000
Fe_s	3.395	0.143	0.286	135.7	65.66	4.302	3.917	0.029
Fe_b	3.294	0.045	0.234	58.98	20.87	3.055	3.004	0.053
Co_s	2.109	0.164	0.274	277.4	38.39	–6.725	9.926	0.037
Co_b	1.977	0.307	–0.011	1.015	56.09	–2.168	4.237	4.174
Nb_s	1.097	0.053	–0.087	21.91	30.36	4.091	16.31	0.769
Nb_b	0.740	0.314	0.049	10.59	488.5	1.028	5.074	0.479
Mo_s	2.678	0.000	0.096	224.5	752.2	0.417	0.568	0.003
Mo_b	2.527	0.012	0.151	323.9	1083	0.454	0.624	0.002
Tc_s	2.493	0.172	0.099	31.64	234.4	0.353	0.509	0.016
Tc_b	2.057	0.059	0.072	12.67	29.32	0.755	1.368	0.111

impurities embedded in two prototypical topological insulators, namely, Bi_2Te_3 and Bi_2Se_3. The simulations were carried out using linear response TD-DFT in the framework of the KKR-GF method, suitable for computing the properties of spin excitations at the nanoscale. A mapping onto a generalized LLG model allowed us to extract from first principles the MAE and transversal components of the Gilbert damping and nutation tensor. The obtained values of the MAE were then compared systematically to the ones obtained using the torque method and band energy differences, that rely on the magnetic force theorem and the frozen potential approximation.

All the considered 3*d* impurities acquire a finite magnetic moment in both hosts, while the strong hybridization of the 4*d* impurities with the host states makes them more sensitive to the surrounding environment. For instance, Ru and Pd were found to be nonmagnetic in Bi_2Te_3 but became magnetic in Bi_2Se_3. Furthermore, and independently from the nature of the orbitals (3*d* or 4*d*), large rotation angles result in significant changes in the electronic properties when a high electronic density of states is found at the Fermi energy, invalidating the assumptions made to invoke the magnetic force theorem. The MAE must be then computed other perturbative methods such as linear response theory or the torque method with small deviation angles. The MAE obtained using linear response theory is found to coincide with the one computed from the torque method at small deviation angles differing only by a negligible renormalization factor.

The spin excitation spectra of the impurities display diverse trends. When the impurity virtual bound states or in-gap states are located away from the Fermi energy, the Gilbert damping is rather low and the lifetime of the excitation reaches high values compared to the ones observed in metallic hosts [20,74]. The most striking example is a Mn impurity in Bi_2Se_3, where the lifetime reaches microseconds. A contrasting situation is observed for Ru, which displays a flat excitation resonance in conjunction with a low lifetime. Moreover, we found that nutation effects can be important and lead to substantial shifts of the resonance frequency for some elements such as Nb, Tc, and Ru. We also examined the contribution of the surface state to the spin dynamics by comparing the LLG parameters of the impurities embedded in the surface with those of impurities embedded in the bulk. For Co and Nb impurities, it was found that the topological surface state has a drastic impact on the dynamics via the spectral shift of the impurity-induced electronic in-gap states, while it plays a minor role for Mn impurities.

The current paper suggests that the in-gap states play a key contribution in tuning the dynamical properties of the impurities, while the topological nature of the energy gap was found to be unimportant. Even if the topological protection of the surface states is lost after scattering at magnetic impurities, their linear dispersion (Dirac-like) may result in other interesting effects as, for example, in the induced Friedel oscillations [75]. The latter are influential when probing dynamical spin excitations of multi-impurity nanostructures [76].

We provided a systematic investigation of the spin dynamics of 3*d* and 4*d* impurities embedded in topologically insulating hosts. The results obtained for excitation lifetimes of some specific impurities (Mn) provide insights on the dual (metal and insulator) nature of these materials. This indicates that these topological materials are of interest in the current search for single-atom based qubits [2,77]. Indeed a pivotal requirement consists in the presence of long coherence times. In addition to that, the MAE computed employing

perturbative methods such as the linear response can be compared to the one extracted from ISTS measurements. Finally, several aspects remain to be uncovered from first principles: the zero-point spin fluctuations [69] of these impurities, which can be accessed via the dynamical magnetic susceptibility, as well as the spin dynamics of magnetic nanoclusters or full magnetic layers deposited on topological insulators.

ACKNOWLEDGMENTS

We thank Dr. Julen Ibañez-Azpiroz for fruitful discussions. This work was supported by the European Research Council (ERC) under the European Union's Horizon 2020 research and innovation programme (ERC Consolidator Grant No. 681405 DYNASORE). We gratefully acknowledge the computing time granted by the JARA-HPC Vergabegremium and VSR commission on the supercomputer JURECA at Forschungszentrum Jülich.

APPENDIX A: PHENOMENOLOGICAL PARAMETERS FROM THE GENERALIZED LANDAU-LIFSHITZ-GILBERT EQUATION

In this Appendix, we provide the explicit forms of the phenomenological quantities (anisotropy field, damping and nutation tensors) discussed in Sec. II C. First, we establish a connection between the anisotropy field $\vec{B}^{\rm a}$ and the magnetocrystalline anisotropy using the phenomenological form of the band energy $\mathcal{E}_{\rm Band}$. For ease of connection with the LLG, we present the derivation using a vector formalism. For systems with uniaxial symmetry, the expansion of the band energy in terms of the magnetization up to second order reads [45]

$$\mathcal{E}_{\rm Band} = \mathcal{E}_0(|\vec{M}|) + \frac{\mathcal{K}}{M^2}\,(\vec{M}\cdot\vec{e}_n)^2 + \ldots. \tag{A1}$$

$\mathcal{E}_0(|\vec{M}|)$ contains the isotropic energy contributions and $\vec{e}_n$ represents the direction of the easy axis. The anisotropy field is then given by the first-order derivative of $\mathcal{E}_{\rm Band}$ with respect to $\vec{M}$ (the longitudinal component does not affect the dynamics within the LLG):

$$\begin{aligned}\vec{B}^{\rm a} &= -\frac{\partial \mathcal{E}_{\rm Band}}{\partial \vec{M}} \\ &= -\frac{2\mathcal{K}}{M^2}\,(\vec{M}\cdot\vec{e}_n)\vec{e}_n.\end{aligned} \tag{A2}$$

Second, the Gilbert damping ($\underline{\mathcal{G}}$) and nutation ($\underline{\mathcal{I}}$) tensors shown in Sec. II C are rank-2 tensors, which can be split into a symmetric part (labeled with the superscript s) and an antisymmetric part (labeled with the superscript a). Moreover, due to the uniaxial symmetry, the Gilbert damping tensor has the following structure:

$$\underline{\mathcal{G}} = -\frac{1}{\gamma M}\begin{pmatrix} \mathcal{G}^s_\parallel & -\mathcal{G}^a_\parallel & \mathcal{G}^a_\perp \\ \mathcal{G}^a_\parallel & \mathcal{G}^s_\parallel & -\mathcal{G}^a_\perp \\ -\mathcal{G}^a_\perp & \mathcal{G}^a_\perp & \mathcal{G}^s_\perp \end{pmatrix}. \tag{A3}$$

The symbol $\parallel$ denotes the spin dynamics parameters describing the transverse components of the precessional motion when the spin moment is along the [111] direction in its ground state. As the system has uniaxial symmetry, the spin dynamics can be anisotropic, and we introduce the symbol $\perp$ to account for this possibility. The nutation tensor has the same structure:

$$\underline{\mathcal{I}} = -\frac{1}{\gamma M}\begin{pmatrix} \mathcal{I}^s_\parallel & -\mathcal{I}^a_\parallel & \mathcal{I}^a_\perp \\ \mathcal{I}^a_\parallel & \mathcal{I}^s_\parallel & -\mathcal{I}^a_\perp \\ -\mathcal{I}^a_\perp & \mathcal{I}^a_\perp & \mathcal{I}^s_\perp \end{pmatrix}. \tag{A4}$$

The previous decomposition of Gilbert damping and nutation tensors is identical to the one performed on magnetic exchange interactions [78,79]. The trace of the damping tensor coincides with the conventional Gilbert damping constant for a cubic system [40], while the off-diagonal components account for the renormalization of γ, which controls the precession rate. Considering the previous forms for the Gilbert damping and nutation combined with Eqs. (9) and (5), the spin-flip dynamical magnetic susceptibility obtained from the LLG equation reads then

$$\chi^{\rm LLG}_{+-}(\omega) = \frac{1}{2}\frac{M\gamma}{-\frac{2\mathcal{K}\gamma}{M} - (1+\mathcal{G}^a_\parallel + i\mathcal{G}^s_\parallel)\,\omega + (-\mathcal{I}^s_\parallel + i\mathcal{I}^a_\parallel)\,\omega^2}. \tag{A5}$$

The resonance frequency is defined as $\frac{\partial {\rm Im}\chi^{\rm LLG}_{+-}(\omega)}{\partial\omega}|_{\omega^{\rm LLG}_{\rm res}} = 0$. In the absence of nutation, it can be computed analytically and is given by

$$\omega^{\rm LLG}_{\rm res} = -\frac{\gamma}{\sqrt{1+(\mathcal{G}^s_\parallel)^2+2\mathcal{G}^a_\parallel+(\mathcal{G}^a_\parallel)^2}}\frac{2\mathcal{K}_{\rm susc}}{M_{\rm s}}. \tag{A6}$$

The latter can be written in terms of the effective gyromagnetic ratio as

$$\omega^{\rm LLG}_{\rm res} = -\frac{\gamma_{\rm eff}}{\sqrt{1+\left(\frac{\mathcal{G}^s_\parallel}{1+\mathcal{G}^a_\parallel}\right)^2}}\frac{2\mathcal{K}_{\rm susc}}{M_{\rm s}}, \quad \text{with} \quad \gamma_{\rm eff} = \frac{\gamma}{1+\mathcal{G}^a_\parallel}. \tag{A7}$$

APPENDIX B: TORQUE METHOD AND LINEAR RESPONSE THEORY

In this Appendix, we consider small deviations of the spin moment from the equilibrium direction and connect the MAE obtained within the torque method and linear response. This will be done employing the retarded single-particle GF, which is defined as the resolvent of the single-particle Hamiltonian $\boldsymbol{\mathcal{H}}(\vec{r}\,)$:

$$[\varepsilon + i0 - \boldsymbol{\mathcal{H}}(\vec{r}\,)]\,\boldsymbol{G}(\vec{r}\,,\vec{r}\,';\varepsilon+i0) = \delta(\vec{r}\,-\vec{r}\,'). \tag{B1}$$

To keep the notation as light as possible, we do not introduce the partition of space into cells around each atom, as is customary in the KKR-GF approach. The expressions can easily be generalized to take that aspect into account. We shall require the following two basic properties (note that the GF is a spin matrix):

$$\begin{aligned}&\frac{\partial}{\partial\varepsilon}\,\boldsymbol{G}(\vec{r}\,,\vec{r}\,';\varepsilon+i0) \\ &\quad = -\int d\vec{r}\,'\,\boldsymbol{G}(\vec{r}\,,\vec{r}\,';\varepsilon+i0)\,\boldsymbol{G}(\vec{r}\,',\vec{r}\,';\varepsilon+i0),\end{aligned} \tag{B2}$$

$$\frac{\partial}{\partial X}\boldsymbol{G}(\vec{r}\,,\vec{r}\,;\varepsilon+i0) = \int d\vec{r}\,'\,\boldsymbol{G}(\vec{r}\,,\vec{r}\,';\varepsilon+i0)\,\frac{\partial \boldsymbol{\mathcal{H}}(\vec{r}\,')}{\partial X}\,\boldsymbol{G}(\vec{r}\,',\vec{r}\,;\varepsilon+i0), \tag{B3}$$

where X is some parameter or quantity upon which the Hamiltonian depends. Both relations follow trivially from the defining equation of the GF [Eq. (B1)]. The electronic density of states is given by

$$\rho(\varepsilon) = -\frac{1}{\pi}\,\mathrm{Im\,Tr}_\sigma \int d\vec{r}\;\; \boldsymbol{G}(\vec{r}\,,\vec{r}\,;\varepsilon+i0), \tag{B4}$$

from which the connection between the GF and the band energy of the main text $\mathcal{E}_{\mathrm{band}}$ is established. The spin magnetization density is given by

$$\vec{M}(\vec{r}\,) = -\frac{1}{\pi}\,\mathrm{Im\,Tr}_\sigma \int_{-\infty}^{\varepsilon_\mathrm{F}} d\varepsilon\;\vec{\boldsymbol{\sigma}}\,\boldsymbol{G}(\vec{r}\,,\vec{r}\,;\varepsilon+i0), \tag{B5}$$

and we make the assumption that the Hamiltonian depends on the direction of the spin magnetization density in a coarse-grained way:

$$\boldsymbol{\mathcal{H}}(\vec{r}\,) = \mathcal{H}_0(\vec{r}\,) + B_\mathrm{xc}(\vec{r}\,)\,\hat{n}(\theta,\varphi)\cdot\vec{\boldsymbol{\sigma}}, \tag{B6}$$

$\hat{n}(\theta,\varphi)$ being the direction of the exchange-correlation magnetic field. Assuming that the easy axis is along the z direction, a small rotation angle θ in the xz plane of $\hat{n}$ results in a torque $\mathcal{T}_\theta$ given in Eq. (14). Using the definition of the band energy and the density of states [Eqs. (13) and (B4)], $\mathcal{T}_\theta$ can be expressed in terms of the GF as

$$\mathcal{T}_\theta = -\frac{1}{\pi}\,\mathrm{Im\,Tr}_\sigma \int d\varepsilon \int d\vec{r}\,(\varepsilon-\varepsilon_\mathrm{F})\,\frac{\partial \boldsymbol{G}(\vec{r}\,,\vec{r}\,;\varepsilon+i0)}{\partial\theta}. \tag{B7}$$

Relying on Eq. (B3), the first-order derivative of the GF with respect to θ can be expressed in terms of the derivative of $\boldsymbol{\mathcal{H}}(\vec{r}\,)$, which reads

$$\begin{aligned}\frac{\partial \boldsymbol{\mathcal{H}}(\vec{r}\,)}{\partial\theta} &= B_\mathrm{xc}(\vec{r}\,)\,\frac{\partial\hat{n}(\theta)}{\partial\theta}\cdot\vec{\boldsymbol{\sigma}}\\ &= B_\mathrm{xc}(\vec{r}\,)[\cos\theta\,\boldsymbol{\sigma}_x - \sin\theta\,\boldsymbol{\sigma}_z].\end{aligned} \tag{B8}$$

The combination of the previous equation with Eqs. (B3) and (B7) leads to the following expression for the torque:

$$\begin{aligned}\mathcal{T}_\theta = -\frac{1}{\pi}\,\mathrm{Im\,Tr}_\sigma \int_{-\infty}^{\varepsilon_\mathrm{F}} d\varepsilon \int d\vec{r}\,B_\mathrm{xc}(\vec{r}\,)[\cos\theta\,\boldsymbol{G}(\vec{r},\vec{r},\varepsilon)\,\boldsymbol{\sigma}_x\\ -\sin\theta\,\boldsymbol{G}(\vec{r},\vec{r},\varepsilon)\,\boldsymbol{\sigma}_z].\end{aligned} \tag{B9}$$

The previous expression was obtained after performing a partial energy integration. Furthermore, considering a small rotation angle, then $\boldsymbol{G}(\vec{r},\vec{r},\varepsilon)$, i.e., the Green's function for the rotated $\vec{B}_\mathrm{xc}$ is related to the unperturbed Green's function $\boldsymbol{G}_0(\vec{r},\vec{r},\varepsilon)$ [with $\vec{B}_\mathrm{xc}(\vec{r})\parallel z$ axis] via a Dyson equation:

$$\begin{aligned}&\boldsymbol{G}(\vec{r},\vec{r},\varepsilon)\\ &\approx \boldsymbol{G}_0(\vec{r},\vec{r},\varepsilon) + \int d\vec{r}\,'\boldsymbol{G}_0(\vec{r},\vec{r}\,',\varepsilon)\,\Delta\vec{B}_\mathrm{xc}(\vec{r}\,')\cdot\vec{\boldsymbol{\sigma}}\,\boldsymbol{G}_0(\vec{r}\,',\vec{r},\varepsilon),\end{aligned} \tag{B10}$$

$\Delta\vec{B}_\mathrm{xc}(\vec{r})$ being the change in the exchange-correlation spin splitting given by

$$\begin{aligned}\Delta\vec{B}_\mathrm{xc}(\vec{r}\,) &= B_\mathrm{xc}(\vec{r}\,)\,(\sin\theta,0,\cos\theta-1)\\ &\approx B_\mathrm{xc}(\vec{r}\,)\left(\theta,0,-\frac{\theta^2}{2}\right).\end{aligned} \tag{B11}$$

Then, the expression of $\boldsymbol{G}(\vec{r},\vec{r},\varepsilon)$ from Eq. (B10) is plugged back into Eq. (B9) and $\cos\theta$ and $\sin\theta$ are expanded for small θ as well (retaining linear terms), resulting in the following form for the torque:

$$\begin{aligned}\mathcal{T}_\theta &= -\frac{1}{\pi}\,\mathrm{Im\,Tr}_\sigma \int_{-\infty}^{\varepsilon_\mathrm{F}} d\varepsilon \int d\vec{r}\,B_\mathrm{xc}(\vec{r}\,)\\ &\quad\times\int d\vec{r}\,'[\boldsymbol{\sigma}_x\,\boldsymbol{G}_0(\vec{r},\vec{r}\,',\varepsilon)B_\mathrm{xc}(\vec{r}\,')\,\boldsymbol{\sigma}_x\,\boldsymbol{G}_0(\vec{r}\,',\vec{r},\varepsilon)]\theta\\ &\quad+\frac{1}{\pi}\,\mathrm{Im\,Tr}_\sigma\int_{-\infty}^{\varepsilon_\mathrm{F}} d\varepsilon\int d\vec{r}\,B_\mathrm{xc}(\vec{r}\,)\boldsymbol{\sigma}_z\,\boldsymbol{G}_0(\vec{r},\vec{r},\varepsilon)\,\theta\\ &= \int d\vec{r}\,B_\mathrm{xc}(\vec{r}\,)\left[\int d\vec{r}\,'\chi_{xx}^\mathrm{KS}(\vec{r},\vec{r}\,',0)\,B_\mathrm{xc}(\vec{r}\,') - M(\vec{r}\,)\right]\theta.\end{aligned} \tag{B12}$$

$\chi_{xx}^\mathrm{KS}(\vec{r},\vec{r}\,',0)$ is the static Kohn-Sham magnetic susceptibility and $M(\vec{r}\,)$ is the magnetization density. Using the definition of the spin-flip Kohn-Sham magnetic susceptibility given in Eq. (5) in the static limit [i.e., $\chi_{xy}^\mathrm{KS}(\vec{r},\vec{r}\,',0) = \chi_{yx}^\mathrm{KS}(\vec{r},\vec{r}\,',0) = 0$, and x and y directions are equivalent due to uniaxial symmetry], the torque reads

$$\mathcal{T}_\theta = \int d\vec{r}\,B_\mathrm{xc}(\vec{r}\,)[2\chi_{+-}^\mathrm{KS}(\vec{r},\vec{r}\,',0)\,B_\mathrm{xc}(\vec{r}\,') - M(\vec{r}\,)]\theta. \tag{B13}$$

The spin splitting and the transversal exchange-correlation kernel $K_\perp^\mathrm{xc}(\vec{r}\,)$ are related via [17,20]

$$B_\mathrm{xc}(\vec{r}\,) = \frac{K_\perp^\mathrm{xc}(\vec{r}\,)M(\vec{r}\,)}{2}. \tag{B14}$$

To obtain a simple result, we coarse grain the exact equations by integrating out the spatial dependence and work with effective scalar quantities. This allows us to write the transversal exchange-correlation kernel as

$$K_\perp^\mathrm{xc} = (\chi_{+-}^\mathrm{KS}(0))^{-1} - \chi_{+-}^{-1}(0). \tag{B15}$$

Plugging the two previous expressions into the coarse-grained form of Eq. (B13), $\mathcal{T}_\theta$ can be written in terms of the static spin-flip magnetic susceptibilities (Kohn-Sham and enhanced) as

$$\mathcal{T}_\theta = -\frac{M^2}{2}[\chi_{+-}^{-1}(0) - \chi_{+-}^\mathrm{KS}(0)\,\chi_{+-}^{-2}(0)]\,\theta. \tag{B16}$$

On one hand, considering that $\chi_{+-}(0)$ (static limit) obtained from TD-DFT relates to $\mathcal{K}_\mathrm{Susc}$ via $\chi_{+-}(0) = \frac{M^2}{4\mathcal{K}_\mathrm{Susc}}$, Eq. (B16) can be recast into

$$\mathcal{T}_\theta = -\left(2\mathcal{K}_\mathrm{Susc} - \frac{8\chi_{+-}^\mathrm{KS}(0)\mathcal{K}_\mathrm{Susc}^2}{M^2}\right)\theta. \tag{B17}$$

On the other hand, the torque $\mathcal{T}_\theta$ is also given by the first-order derivative of the phenomenological form of the band energy as

$$\mathcal{T}_\theta = \frac{\partial \mathcal{E}_{\text{Band}}}{\partial \theta} = -\mathcal{K}_{\text{Torque}} \sin 2\theta. \tag{B18}$$

After expanding for a small angle, $\mathcal{T}_\theta$ reads

$$\mathcal{T}_\theta = -2\,\mathcal{K}_{\text{Torque}}\,\theta. \tag{B19}$$

The connection between $\mathcal{K}_{\text{Torque}}$ and $\mathcal{K}_{\text{Susc}}$ shown in Eq. (16) of the main text can be established when comparing Eqs. (B17) and (B19).

[1] Y. Shiroishi, K. Fukuda, I. Tagawa, H. Iwasaki, S. Takenoiri, H. Tanaka, H. Mutoh, and N. Yoshikawa, Future options for HDD storage, IEEE Trans. Magn. **45**, 3816 (2009).

[2] F. D. Natterer, K. Yang, W. Paul, P. Willke, T. Choi, T. Greber, A. J. Heinrich, and C. P. Lutz, Reading and writing single-atom magnets, Nature (London) **543**, 226 (2017).

[3] A. J. Heinrich, J. A. Gupta, C. P. Lutz, and D. M. Eigler, Single-atom spin-flip spectroscopy, Science **306**, 466 (2004).

[4] B. Bryant, A. Spinelli, J. J. T. Wagenaar, M. Gerrits, and A. F. Otte, Local Control of Single Atom Magnetocrystalline Anisotropy, Phys. Rev. Lett. **111**, 127203 (2013).

[5] J. C. Oberg, M. R. Calvo, F. Delgado, M. Moro-Lagares, D. Serrate, D. Jacob, J. Fernández-Rossier, and C. F. Hirjibehedin, Control of single-spin magnetic anisotropy by exchange coupling, Nat. Nanotechnol. **9**, 64 (2013).

[6] J. Fernández-Rossier, Theory of Single-Spin Inelastic Tunneling Spectroscopy, Phys. Rev. Lett. **102**, 256802 (2009).

[7] S. Loth, K. von Bergmann, M. Ternes, A. F. Otte, C. P. Lutz, and A. J. Heinrich, Controlling the state of quantum spins with electric currents, Nat. Phys. **6**, 340 (2010).

[8] T. Balashov, T. Schuh, A. F. Takács, A. Ernst, S. Ostanin, J. Henk, I. Mertig, P. Bruno, T. Miyamachi, S. Suga, and W. Wulfhekel, Magnetic Anisotropy and Magnetization Dynamics of Individual Atoms and Clusters of Fe and Co on Pt(111), Phys. Rev. Lett. **102**, 257203 (2009).

[9] A. A. Khajetoorians, S. Lounis, B. Chilian, A. T. Costa, L. Zhou, D. L. Mills, J. Wiebe, and R. Wiesendanger, Itinerant Nature of Atom-Magnetization Excitation by Tunneling Electrons, Phys. Rev. Lett. **106**, 037205 (2011).

[10] B. Chilian, A. A. Khajetoorians, S. Lounis, A. T. Costa, D. L. Mills, J. Wiebe, and R. Wiesendanger, Anomalously large g factor of single atoms adsorbed on a metal substrate, Phys. Rev. B **84**, 212401 (2011).

[11] A. A. Khajetoorians, T. Schlenk, B. Schweflinghaus, M. dos Santos Dias, M. Steinbrecher, M. Bouhassoune, S. Lounis, J. Wiebe, and R. Wiesendanger, Spin Excitations of Individual Fe Atoms on Pt(111): Impact of the Site-Dependent Giant Substrate Polarization, Phys. Rev. Lett. **111**, 157204 (2013).

[12] F. Donati, Q. Dubout, G. Autès, F. Patthey, F. Calleja, P. Gambardella, O. V. Yazyev, and H. Brune, Magnetic Moment and Anisotropy of Individual Co Atoms on Graphene, Phys. Rev. Lett. **111**, 236801 (2013).

[13] J. Honolka, A. A. Khajetoorians, V. Sessi, T. O. Wehling, S. Stepanow, J. L. Mi, B. B. Iversen, T. Schlenk, J. Wiebe, N. B. Brookes, A. I. Lichtenstein, Ph. Hofmann, K. Kern, and R. Wiesendanger, In-Plane Magnetic Anisotropy of Fe Atoms on Bi_2Se_3(111), Phys. Rev. Lett. **108**, 256811 (2012).

[14] P. Gambardella, S. Rusponi, M. Veronese, S. S. Dhesi, C. Grazioli, A. Dallmeyer, I. Cabria, R. Zeller, P. H. Dederichs, K. Kern, C. Carbone, and H. Brune, Giant magnetic anisotropy of single Cobalt atoms and nanoparticles, Science **300**, 1130 (2003).

[15] J. Fransson, Spin inelastic electron tunneling spectroscopy on local spin adsorbed on surface, Nano Lett. **9**, 2414 (2009).

[16] J. Fransson, H. C. Manoharan, and A. V. Balatsky, Detection and cloaking of molecular objects in coherent nanostructures using inelastic electron tunneling spectroscopy, Nano Lett. **10**, 1600 (2010).

[17] S. Lounis, A. T. Costa, R. B. Muniz, and D. L. Mills, Dynamical Magnetic Excitations of Nanostructures from First Principles, Phys. Rev. Lett. **105**, 187205 (2010).

[18] S. Lounis, A. T. Costa, R. B. Muniz, and D. L. Mills, Theory of local dynamical magnetic susceptibilities from the Korringa-Kohn-Rostoker Green function method, Phys. Rev. B **83**, 035109 (2011).

[19] S. Lounis, B. Schweflinghaus, M. dos Santos Dias, M. Bouhassoune, R. B. Muniz, and A. T. Costa, Theoretical probing of inelastic spin-excitations in adatoms on surfaces, Surf. Sci. **630**, 317 (2014).

[20] M. dos Santos Dias, B. Schweflinghaus, S. Blügel, and S. Lounis, Relativistic dynamical spin excitations of magnetic adatoms, Phys. Rev. B **91**, 075405 (2015).

[21] E. K. U. Gross and W. Kohn, Local Density-Functional Theory of Frequency-Dependent Linear Response, Phys. Rev. Lett. **55**, 2850 (1985).

[22] M. Z. Hasan and C. L. Kane, Colloquium: Topological insulators, Rev. Mod. Phys. **82**, 3045 (2010).

[23] X.-L. Qi and S.-C. Zhang, Topological insulators and superconductors, Rev. Mod. Phys. **83**, 1057 (2011).

[24] H. Zhang, C.-X. Liu, X.-L. Qi, X. Dai, Z. Fang, and S.-C. Zhang, Topological insulators in Bi_2Se_3, Bi_2Te_3 and Sb_2Te_3 with a single Dirac cone on the surface, Nat. Phys. **5**, 438 (2009).

[25] T. Eelbo, M. Waśniowska, M. Sikora, M. Dobrzański, A. Kozłowski, A. Pulkin, G. Autès, I. Miotkowski, O. V. Yazyev, and R. Wiesendanger, Strong out-of-plane magnetic anisotropy of fe adatoms on Bi_2Te_3, Phys. Rev. B **89**, 104424 (2014).

[26] T. Schlenk, M. Bianchi, M. Koleini, A. Eich, O. Pietzsch, T. O. Wehling, T. Frauenheim, A. Balatsky, J.-L. Mi, B. B. Iversen, J. Wiebe, A. A. Khajetoorians, Ph. Hofmann, and R. Wiesendanger, Controllable Magnetic Doping of the Surface State of a Topological Insulator, Phys. Rev. Lett. **110**, 126804 (2013).

[27] D. West, Y. Y. Sun, S. B. Zhang, T. Zhang, X. Ma, P. Cheng, Y. Y. Zhang, X. Chen, J. F. Jia, and Q. K. Xue, Identification of magnetic dopants on the surfaces of topological insulators: Experiment and theory for Fe on Bi_2Te_3(111), Phys. Rev. B **85**, 081305(R) (2012).

[28] P. Sessi, R. R. Biswas, T. Bathon, O. Storz, S. Wilfert, A. Barla, K. A. Kokh, O. E. Tereshchenko, K. Fauth, M. Bode *et al.*, Dual nature of magnetic dopants and competing trends in topological insulators, Nat. Commun. **7**, 12027 (2016).

[29] C.-X. Liu, S.-C. Zhang, and X.-L Qi, The quantum anomalous hall effect: Theory and experiment, Annu. Rev. Condens. Matter Phys. **7**, 301 (2016).

[30] M. F. Islam, C. M. Canali, A. Pertsova, A. Balatsky, S. K. Mahatha, C. Carbone, A. Barla, K. A. Kokh, O. E. Tereshchenko, E. Jiménez, N. B. Brookes, P. Gargiani, M. Valvidares, S. Schatz, T. R. F. Peixoto, H. Bentmann, F. Reinert, J. Jung, T. Bathon, K. Fauth, M. Bode, and P. Sessi, Systematics of electronic and magnetic properties in the transition metal doped Sb_2Te_3 quantum anomalous hall platform, Phys. Rev. B **97**, 155429 (2018).

[31] T. Yokoyama, J. Zang, and N. Nagaosa, Theoretical study of the dynamics of magnetization on the topological surface, Phys. Rev. B **81**, 241410(R) (2010).

[32] Y. Tserkovnyak and D. Loss, Thin-Film Magnetization Dynamics on the Surface of a Topological Insulator, Phys. Rev. Lett. **108**, 187201 (2012).

[33] I. Garate and M. Franz, Inverse Spin-Galvanic Effect in the Interface Between a Topological Insulator and a Ferromagnet, Phys. Rev. Lett. **104**, 146802 (2010).

[34] H. T. Ueda, A. Takeuchi, G. Tatara, and T. Yokoyama, Topological charge pumping effect by the magnetization dynamics on the surface of three-dimensional topological insulators, Phys. Rev. B **85**, 115110 (2012).

[35] B. Dóra and F. Simon, Unusual spin dynamics in topological insulators, Sci. Rep. **5**, 14844 (2015).

[36] L. Chotorlishvili, A. Ernst, V. K. Dugaev, A. Komnik, M. G. Vergniory, E. V. Chulkov, and J. Berakdar, Magnetic fluctuations in topological insulators with ordered magnetic adatoms: Cr on Bi_2Se_3 from first principles, Phys. Rev. B **89**, 075103 (2014).

[37] T. M. Garitezi, G. G. Lesseux, C. B. R. Jesus, T. Grant, Z. Fisk, R. R. Urbano, C. Rettori, and P. G. Pagliuso, Electron spin resonance of Gd^{3+} in three dimensional topological insulator Bi_2Se_3, J. Phys.: Conf. Ser. **592**, 012125 (2015).

[38] B. Schweflinghaus, M. dos Santos Dias, A. T. Costa, and S. Lounis, Renormalization of electron self-energies via their interaction with spin excitations: A first-principles investigation, Phys. Rev. B **89**, 235439 (2014).

[39] J. Bouaziz, M. dos Santos Dias, J. Ibañez-Azpiroz, and S. Lounis, Ab initio investigation of impurity-induced in-gap states in Bi_2Te_3 and Bi_2Se_3, Phys. Rev. B **98**, 035119 (2018).

[40] T. L. Gilbert, A phenomenological theory of damping in ferromagnetic materials, IEEE Trans. Magn. **40**, 3443 (2004).

[41] S. Bhattacharjee, L. Nordström, and J. Fransson, Atomistic Spin Dynamic Method with Both Damping and Moment of Inertia Effects Included from First Principles, Phys. Rev. Lett. **108**, 057204 (2012).

[42] A. Oswald, R. Zeller, P. J. Braspenning, and P. H. Dederichs, Interaction of magnetic impurities in Cu and Ag, J. Phys. F **15**, 193 (1985).

[43] A. I. Liechtenstein, M. I. Katsnelson, V. P. Antropov, and V. A. Gubanov, Local spin density functional approach to the theory of exchange interactions in ferromagnetic metals and alloys, J. Magn. Magn. Mater. **67**, 65 (1987).

[44] G. H. O. Daalderop, P. J. Kelly, and M. F. H. Schuurmans, First-principles calculation of the magnetocrystalline anisotropy energy of iron, cobalt, and nickel, Phys. Rev. B **41**, 11919 (1990).

[45] X. Wang, R. Wu, D. S. Wang, and A. J. Freeman, Torque method for the theoretical determination of magnetocrystalline anisotropy, Phys. Rev. B **54**, 61 (1996).

[46] R. A. Sack, Relaxation processes and inertial effects I: Free rotation about a fixed axis, Proc. Phys. Soc. London, Sect. B **70**, 402 (1957).

[47] M.-C. Ciornei, J. M. Rubí, and J.-E. Wegrowe, Magnetization dynamics in the inertial regime: Nutation predicted at short time scales, Phys. Rev. B **83**, 020410(R) (2011).

[48] S. Lounis, M. dos Santos Dias, and B. Schweflinghaus, Transverse dynamical magnetic susceptibilities from regular static density functional theory: Evaluation of damping and g shifts of spin excitations, Phys. Rev. B **91**, 104420 (2015).

[49] N. Papanikolaou, R. Zeller, and P. H. Dederichs, Conceptual improvements of the KKR method, J. Phys.: Condens. Matter **14**, 2799 (2002).

[50] D. S. G. Bauer, Development of a relativistic full-potential first-principles multiple scattering Green function method applied to complex magnetic textures of nano structures at surfaces, Ph.D. thesis, Forschungszentrum Jülich, 2014, http://publications.rwth-aachen.de/record/229375.

[51] S. H. Vosko, L. Wilk, and M. Nusair, Accurate spin-dependent electron liquid correlation energies for local spin density calculations: a critical analysis, Can. J. Phys. **58**, 1200 (1980).

[52] W. Zhang, R. Yu, H.-J. Zhang, X. Dai, and Z. Fang, First-principles studies of the three-dimensional strong topological insulators Bi_2Te_3, Bi_2Se_3 and Sb_2Te_3, New J. Phys. **12**, 065013 (2010).

[53] L. B. Abdalla, L. Seixas, T. M. Schmidt, R. H. Miwa, and A. Fazzio, Topological insulator Bi_2Se_3(111) surface doped with transition metals: An ab initio investigation, Phys. Rev. B **88**, 045312 (2013).

[54] J.-M. Zhang, W. Ming, Z. Huang, G.-B. Liu, X. Kou, Y. Fan, K. L. Wang, and Y. Yao, Stability, electronic, and magnetic properties of the magnetically doped topological insulators Bi_2Se_3, Bi_2Te_3, and Sb_2Te_3, Phys. Rev. B **88**, 235131 (2013).

[55] K. L. Liu and S. H. Vosko, A time-dependent spin density functional theory for the dynamical spin susceptibility, Can. J. Phys. **67**, 1015 (1989).

[56] D. Böttcher and J. Henk, Significance of nutation in magnetization dynamics of nanostructures, Phys. Rev. B **86**, 020404(R) (2012).

[57] D. Thonig, O. Eriksson, and M. Pereiro, Magnetic moment of inertia within the torque-torque correlation model, Sci. Rep. **7**, 931 (2017).

[58] R. Mondal, M. Berritta, A. K. Nandy, and P. M. Oppeneer, Relativistic theory of magnetic inertia in ultrafast spin dynamics, Phys. Rev. B **96**, 024425 (2017).

[59] X. Wang, D.-s. Wang, R. Wu, and A. J. Freeman, Validity of the force theorem for magnetocrystalline anisotropy, J. Magn. Magn. Mater. **159**, 337 (1996).

[60] S. Lounis, Ph. Mavropoulos, P. H. Dederichs, and S. Blügel, Noncollinear Korringa-Kohn-Rostoker Green function method: Application to 3d nanostructures on Ni(001), Phys. Rev. B **72**, 224437 (2005).

[61] J. B. Staunton, L. Szunyogh, A. Buruzs, B. L. Gyorffy, S. Ostanin, and L. Udvardi, Temperature dependence of magnetic

anisotropy: An ab initio approach, Phys. Rev. B **74**, 144411 (2006).

[62] S. Mankovsky, S. Bornemann, J. Minár, S. Polesya, H. Ebert, J. B. Staunton, and A. I. Lichtenstein, Effects of spin-orbit coupling on the spin structure of deposited transition-metal clusters, Phys. Rev. B **80**, 014422 (2009).

[63] P. Bruno, Exchange Interaction Parameters and Adiabatic Spin-Wave Spectra of Ferromagnets: A "Renormalized Magnetic Force Theorem," Phys. Rev. Lett. **90**, 087205 (2003).

[64] F. S. M. Guimarães, M. dos Santos Dias, B. Schweflinghaus, and S. Lounis, Engineering elliptical spin-excitations by complex anisotropy fields in Fe adatoms and dimers on Cu(111), Phys. Rev. B **96**, 144401 (2017).

[65] M. Michiardi, I. Aguilera, M. Bianchi, V. E. de Carvalho, L. O. Ladeira, N. G. Teixeira, E. A. Soares, C. Friedrich, S. Blügel, and P. Hofmann, Bulk band structure of Bi_2Te_3, Phys. Rev. B **90**, 075105 (2014).

[66] E. Mooser and W. B. Pearson, New semiconducting compounds, Phys. Rev. **101**, 492 (1956).

[67] J. Black, E. M. Conwell, L. Seigle, and C. W. Spencer, Electrical and optical properties of some $M_2^{V-B}N_3^{VI-B}$ semiconductors, J. Phys. Chem. Solids **2**, 240 (1957).

[68] J. F. Janak, Uniform susceptibilities of metallic elements, Phys. Rev. B **16**, 255 (1977).

[69] J. Ibañez-Azpiroz, M. dos Santos Dias, S. Blügel, and S. Lounis, Zero-point spin-fluctuations of single adatoms, Nano Lett. **16**, 4305 (2016).

[70] P. Bruno, Tight-binding approach to the orbital magnetic moment and magnetocrystalline anisotropy of transition-metal monolayers, Phys. Rev. B **39**, 865 (1989).

[71] Š. Pick, V. S. Stepanyuk, A. N. Baranov, W. Hergert, and P. Bruno, Effect of atomic relaxations on magnetic properties of adatoms and small clusters, Phys. Rev. B **68**, 104410 (2003).

[72] C. F. Hirjibehedin, C. P. Lutz, and A. J. Heinrich, Spin coupling in engineered atomic structures, Science **312**, 1021 (2006).

[73] C. F. Hirjibehedin, C. Y. Lin, A. F. Otte, M. Ternes, C. P. Lutz, B. A. Jones, and A. J. Heinrich, Large magnetic anisotropy of a single atomic spin embedded in a surface molecular network, Science **317**, 1199 (2007).

[74] J. I. Azpiroz, M. dos Santos Dias, S. Blügel, and S. Lounis, Longitudinal and transverse spin relaxation times of magnetic single adatoms: An ab initio analysis, Phys. Rev. B **96**, 144410 (2017).

[75] R. R. Biswas and A. V. Balatsky, Impurity-induced states on the surface of three-dimensional topological insulators, Phys. Rev. B **81**, 233405 (2010).

[76] M. Steinbrecher, R. Rausch, K. T. That, J. Hermenau, A. A. Khajetoorians, M. Potthoff, R. Wiesendanger, and J. Wiebe, Non-collinear spin states in bottom-up fabricated atomic chains, Nat. Commun. **9**, 2853 (2018).

[77] F. D. Natterer, F. Donati, F. Patthey, and H. Brune, Thermal and Magnetic-Field Stability of Holmium Single-Atom Magnets, Phys. Rev. Lett. **121**, 027201 (2018).

[78] L. Udvardi, L. Szunyogh, K. Palotás, and P. Weinberger, First-principles relativistic study of spin waves in thin magnetic films, Phys. Rev. B **68**, 104436 (2003).

[79] H. Ebert and S. Mankovsky, Anisotropic exchange coupling in diluted magnetic semiconductors: Ab initio spin-density functional theory, Phys. Rev. B **79**, 045209 (2009).